ISSN 1063-7834, Physics of the Solid State, 2019, Vol. 61, No. 4, pp. 618–626. © Pleiades Publishing, Ltd., 2019.

OPTICAL
PROPERTIES

Temperature Dependent Raman Spectroscopic Study of the Fe Doped $La_{0.67}Sr_{0.33}MnO_3$ Prepared Using Ball Milling Method

Nidhi Astik[a, *], **Prafulla K. Jha**[a], **and Vasant Sathe**[b]
[a] *Department of Physics, The M. S. University of Baroda, Vadodara, Gujarat, India*
[b] *UGC-DAE Consortium for Scientific Research, University Campus, Khandwa Road, Indore, India*
**e-mail: nidhiastik2002@gmail.com*

Received June 21, 2018; revised October 15, 2018; accepted October 30, 2018

Abstract—Polycrystalline samples of $La_{0.67}Sr_{0.33}Mn_{0.65}Fe_{0.35}O_3$ (LSMFO) were synthesized using the standard ball mill method with different calcination temperatures ranging from 800 to 1100°C for 7 h. The phase purity of these samples was confirmed using X-ray diffraction (XRD) patterns. All samples were found to have rhombohedral crystal structure with $R\bar{3}c$ space group. The lattice parameters, cell volume, bond angle and bond length have been obtained using the Rietveld refinement by FullProf software. The average crystallite size calculated using the Debye-Scherrer formula was found between 27 and 60 nm. Surface morphology of the prepared samples has been examined using a scanning electron microscope (SEM). SEM images show the formation of well-arranged grain sizes distributed from 240 to 400 nm, much larger than one estimated using the Scherrer formula. All tiny particles are highly agglomerated with the increasing temperature and porosity decreases with increasing temperature. An analysis of the frequency and peak broadening of Raman modes as a function of temperature clearly shows the significant temperature effect on the A_{1g} and E_g modes of LSMFO. The shifts and broadening of the A_{1g} and E_g modes are discussed in light of the oxygen sublattice distortion. Our study shows the reduction in distortion with increasing calcination temperature, which suggests a decrease in the JT effect.

DOI: 10.1134/S1063783419040036

1. INTRODUCTION

For many years, extensive studies have been performed to understand the nature of the bulk as well as thin film samples of perovskite manganese oxides of the form $R_{1-x}A_xMnO_3$ (where R is a rare earth ion and A is a divalent alkali earth ion) particularly after the discovery of colossal magnetoresistance (CMR) in them [1–8]. In this regard, $La_{1-x}Sr_xMnO_3$ (LSMO) has attracted most attention due to its excellent catalytic, thermal, electrical and magnetic properties useful for potential applications in magnetic sensors, reading heads for magnetic memories and as a cathode in solid oxide fuel cells [9–13]. Furthermore, these manganites exhibit puzzling properties arising from the coupling of spin, lattice, charge and structural degrees of freedom and are governed by several factors such as method of preparation, percentage and size of divalent ions. Several methods such as the coprecipitation or precipitation, sol–gel, ball milling and the combustion conventional ceramic are often used to prepare these materials. The mechanical ball milling method is an efficient technique to synthesize many unique materials such as nanostructured crystalline, amorphous alloys and nanoparticles from powder oxides due to high flexibility, simple control of process parameters and ability to produce a wide range of materials [14]. A number of consideration such as double exchange (DE) and superexchange (SE) interactions, Jahn–Teller distortion with electron-phonon interaction and polaron formation, phase separation and site disorder have been used to explain the CMR, one of the most exciting phenomena of manganites [15]. However, a disagreement on the theoretical explanation of CMR behaviour suggests inclusion of something beyond these due to involved complexities [16].

It is established that the properties of manganites are highly influenced by the degree of compositional flexibility such as A-site and B-site doping [17–20]. The A (rare-earth) site doping is the doping of another ion A' with a valence different from A, while B (manganese) site doping is the partial substitution of B ions by another ion B' of different valence. The electronic structure of manganites shows a core spin of 3/2 for Mn ions and an extra e_g electron with its spin aligned to the core electron due to strong exchange for a dopant dependent fraction $(1 - x)$ [21]. These electrons may coherently hop of such electrons to the adjacent sites by means of polarization conserving process. One of the two most successful theories to explain the CMR and related properties is the double exchange theory which considers the magnetic coupling between Mn^{3+} and Mn^{4+} ions [22]. The amount of the pairs of Mn^{3+} and Mn^{4+} depends on the doping level of the perovskite or its oxygen stoichiometry. However, this doping results in a distortion of the perovskite structure with direct influence on the Mn—O bond length and Mn^{3+}—O—Mn^{4+} bond angle [22]. It is noteworthy that the ferromagnetic (FM) coupling and the metal insulator (MI) transition temperature strongly depend on these parameters [23]. Therefore, it is expected that any change at B-site may result into the disorder and hence changes in transport and magnetic properties due to modification of the Mn^{3+}—O^{2-}—Mn^{4+} arrangement [24]. This suggest that the ionic size and valence states of the element being used to substitute Mn ion play a pivotal role in determining various properties of manganites. Many studies have been carried out with different B-site substitution such as Fe, Ru, Cr, Co, Ni, Cu etc. to see their effects on the ferromagnetic (FM)—paramagnetic (PM) transition peak (T_C) and other properties [25—29]. The disorder arising from the doping at the manganese site which influences the CMR properties is directly linked to the crystal structure and the chemical bonds. Hao et al. [30] found that the magnetic ion doped LSMO samples can be described by mixed phases of rhombohedral lattice ($R\bar{3}c$) and orthorhombic ($Pnma$). The neutron diffraction studies indicate the existence of a mixed valence state for the TM ions [31, 32]. The doping of Co ion at the Mn site of LSMO shows the presence of a large number of magnetic species [32]. Despite an importance and long history of Mn substitution studies, the Fe substitution at Mn site is comparatively less explored [16]. Mostafa et al. [33] have performed the Mossbauer spectroscopy and electrical resistivity measurements of $La_{0.7}Sr_{0.3}Mn_{1-x}Fe_xO_3$ for x ranging from 0.3 to 0.7 and found that the substitution of Mn^{3+} by Fe^{3+} suppress the DE and reduces the metal—insulator (MI) transition temperature and flux density saturation. Ahn et al. [34] observed that the Fe doping at Mn site encourages and discourages respectively the anti-ferromagnetic and ferromagnetic behaviors and suppresses the double exchange effect. Cai et al. [35] also observed the similar results on the suppression of DE with 10% Fe doping in $La_{0.7}Ca_{0.3}Mn_1O_3$ (LCMO). Liu et al. [36] found that the Fe doping at Mn site of $Pb_{0.75}Sr_{0.25}MnO_3$ (PCMO) results in the percolation of magnetic polarons above T_C in an insulating PM phase. It is also observed from the resistivity measurement that the Fe doping decreases T_C like T_{MI} [37]. Therefore an extensive work on these systems is still required [16]. The substitution of Fe at Mn site is of particular interest because of the large extent to which it can replace Mn without any structural deformation due to having very close ionic radii.

2. METHODOLOGY

A series of $La_{0.7}Sr_{0.3}Mn_{1-x}Fe_xO_3$ $x = 0.35$ compounds were prepared using the standard planetary ball milling method based on a solid state reaction (SSR) of high purity (99.99%) starting compounds of La_2O_3, SrO, MnO_2, and Fe_2O_3. All chemicals were of analytical grade purchased from Sigma Aldrich and used without any further purification. These compounds were thoroughly mixed in air in a ball milling unit for 7 h and then fired at different calcination temperatures such as 800, 900, 1000, and 1100°C for 7 to 8 h. The rotation speed was chosen to be 250 rpm while the ball to powder ratio was 10 : 1 [38]. The crystallographic information of the grown phase was obtained by powder X-ray diffraction (XRD) patterns at room temperature using PANalytical X'pert Pro diffractometer with CuK_α radiation (λ = 1.5406 Å). The elemental analysis and surface morphology of the resulting products were investigated using a JEOL JMS-5610LV scanning electron microscope equipped with Oxford INCA Energy Dispersive analysis of x-rays (EDAX). The Raman spectra of the Fe doped LSMO samples were recorded with JOBIN HORIBA—HR800.

3. RESULTS AND DISCUSSION

The phase, lattice symmetry and unit cell parameters of the $La_{0.7}Sr_{0.3}Mn_{0.65}Fe_{0.35}O_3$ (LSMFO) samples were determined using powder X-ray diffraction. Figure 1 shows the Rietveld refined X-ray diffraction (XRD) patterns of LSMFO Perovskite manganites for calcination temperatures 800, 900, 1000, and 1100°C. The XRD data were collected by a step scanning over the 2θ range from 20° to 80° at a step size of 0.02 [39, 40] and analyzed by the Rietveld method using FullProf program [41]. The program permits multiple phase refinements of each coexisting phase [42]. The LSMFO samples calcined at different temperatures crystallize in the rhombohedral structure with $R\bar{3}c$ (D^6_{3d}) space group. A secondary phase for the sample calcined at 800°C and 900°C has been observed, which can be attributed to the unreacted Mn_3O_4 [43, 44]. We do not observe any unfitted peaks in the difference pattern [43]. The 1000°C and 1100°C calcined LSMFO samples crystallize in the single phase rhombohedral crystal structure with all diffraction peaks fitted. This shows that the increase in calcination temperature helps in vanishing impurity and completing reaction. In addition, the width of the diffraction peaks narrows suggesting an increase in average particle size [45]. The average crystallite size has been calculated using the Debye Scherrer formula $D = K\lambda/\beta\cos\theta$, where λ, θ, β, and K respectively are the

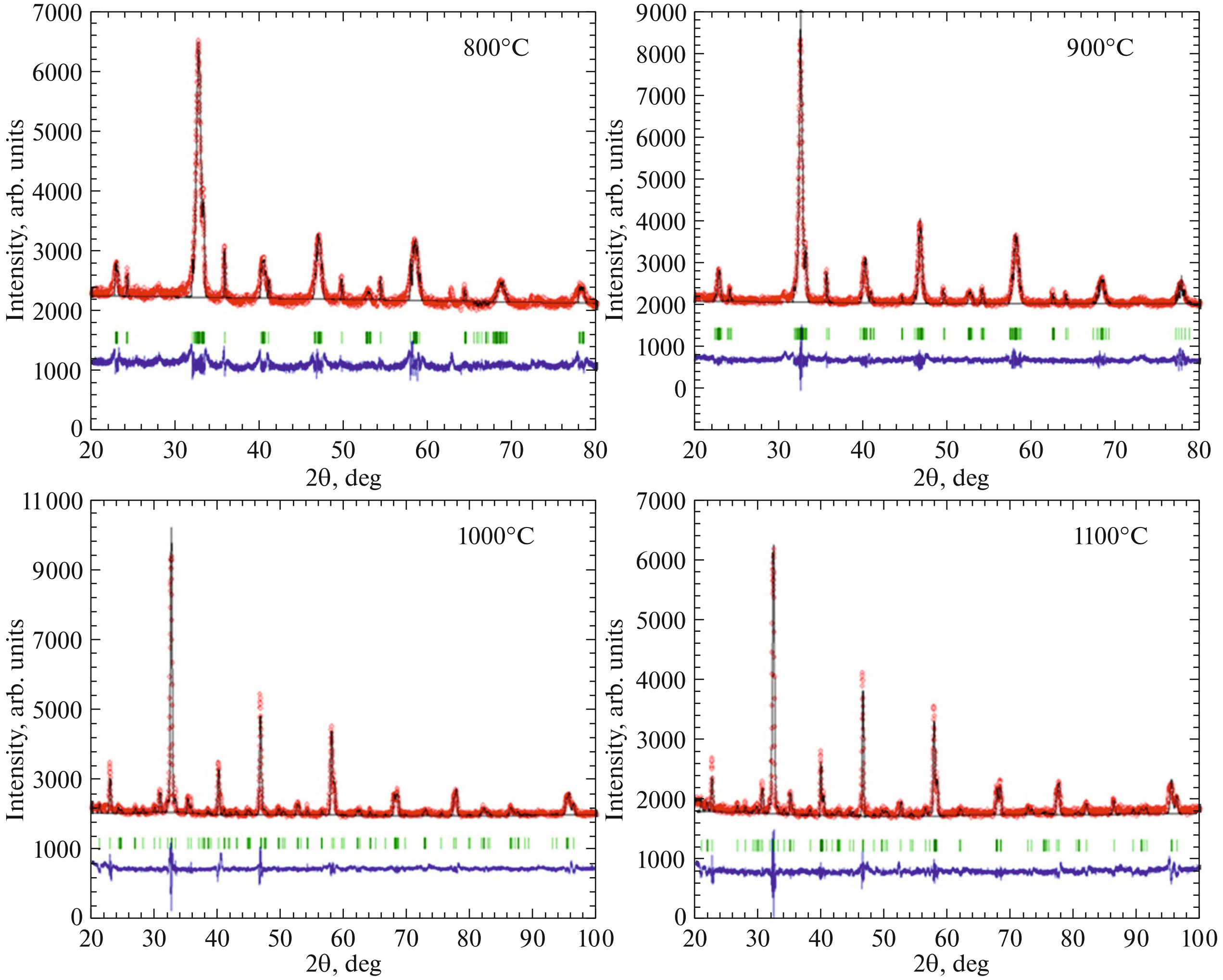

Fig. 1. Rietveld refinements XRD analysis of $La_{0.67}Sr_{0.33}Mn_{1-x}Fe_xO_3$ ($x = 0.35$) at different calcinations temperatures ($T = 800$ to 1100°C).

wavelength of the X-ray, Bragg's angle, full width half-maximum (FWHM) and shape factor which is usually 0.9. The intensity of the diffraction peaks for the perovskite phase increases with the increase in calcination temperature indicating better crystallinity of LSMFO and increase and decrease in the particle size and cell volume respectively (Table 1) consistent with earlier reports [46, 47]. The shift of the (104) peak towards a higher value of the Bragg angle indicates decrease in lattice parameters upon increasing the calcination temperature. The structural parameters such as unit cell volume, lattice parameter, crystallite size and fitting parameters R_p, R_{wp}, R_e, and χ^2 are summarized in Table 1. It is noteworthy that the crystal structure does not change with Fe substitution for Mn in LSMO which is consistent with earlier reports. A substitution of 5% Fe or Cr for Mn in the FM metallic $La_{0.67}Sr_{0.33}MnO_3$ shows no change in the structure due to their similar ionic radii [30, 48–50]. The Mn–O bond length and Mn–O–Mn bond angle presented in Table 1 decreases and increases respectively up to 1000°C but show reverse trend for calcination temperature of 1100°C. This implies that the rhombohedral distortion of the lattice decreases or remains almost same.

Figure 2 displays surface morphology of the LSMFO which shows that the Fe doped LSMO samples are in the submicron range. The SEM images further reveal a nonuniform distribution of grains for all samples and increase in grain size with increasing temperature [51]. A careful analysis of SEM images reveals well defined grains with clear boundaries. Agglomeration of tiny particles with the distance scale of 5 μm is clearly seen in SEM images. It is further to note that the LSMFO samples without any intermediate grinding process cause irregular grain formation due to the homogeneity of agglomerated particles [46, 52]. It is also observed that the porosity of the LSMFO reduces

Table 1. Rietveld refinement structural parameters of $La_{0.67}Sr_{0.33}Mn_{1-x}Fe_xO_3$ at different calcination temperature

Sample	$x = 0.35$ (800°C)	(900°C)	(1000°C)	(1100°C)
Structure type	Rhombohedral	Rhombohedral	Rhombohedral	Rhombohedral
Space group	$R\bar{3}c$	$R\bar{3}c$	$R\bar{3}c$	$R\bar{3}c$
Profile fitting function	Pseudo-Voigt	Pseudo-Voigt	Pseudo-Voigt	Pseudo-Voigt
Lattice Parameter				
a (Å)	5.512	5.538	5.430	5.443
b (Å)	5.512	5.538	5.430	5.443
c (Å)	13.59	13.47	13.21	13.20
V (Å^3)	357.8	357.9	338.5	338.8
La/Sr (6a)				
x	0.000	0.000	0.000	0.000
y	0.000	0.000	0.000	0.000
z	0.25	0.25	0.25	0.25
Mn/Fe (6b)				
x	0.000	0.000	0.000	0.000
y	0.000	0.000	0.000	0.000
z	0.000	0.000	0.000	0.000
O (18e)				
x	0.535	0.458	0.453	0.461
y	0.000	0.000	0.000	0.000
z	0.25	0.25	0.25	0.25
Mn–O–Mn, deg	164.87	166.42	167.37	164.81
Mn–O, Å	1.974	1.968	1.930	1.963
Discrepancy factor (%)				
R_{wp}	27.3	24.0	23.4	25.0
R_p	67.1	54.8	38.1	56.5
R_{exp}	16.1	13.3	13.4	19.3
Goodness of Fit (χ^2)	1.69	1.80	1.74	1.29
Particle size (nm)	27	34	54	60

with increasing calcination temperature [53]. The grain size is ranging between 240–400 nm which is larger than the crystallite size obtained from XRD. This difference may be due to the fact that the grains are composed of several crystallites probably due to the internal stress or defects in the structure [51, 54]. The EDAX spectra presented in Fig. 3 confirm the presence of all elements in all samples. The molar ratio of La, Sr, Mn, Fe, and O presented in Table 2 suggests near stoichiometricity of LSMFO samples. Furthermore, no additional impurity peak in any of the spectra implies pure nature of the prepared samples [55]. Figures 4a, 4b present the room and low (80 K) temperature Raman spectra collected using 632.8 nm excitation wave length in the frequency interval of 200–800 cm^{-1} for Fe doped $La_{0.67}Sr_{0.3}MnO_3$ compounds calcined at four temperatures 800, 900, 1000, and 1100°C for 7 h. The LSMFO samples crystallize in rhombohedral crystal structure with the space group D_{3d}^{6}, $Z = 2$. This structure can be obtained from the simple cubic perovskite by the rotation of adjacent MnO_6 octahedra in the opposite direction around the $[111]_c$ cubic direction [56]. The details of the Raman spectra and possible modes for rhombohedral crystal structure are discussed in [56]. According to the site group analysis, there are 30 vibrational modes: $2A_{1u} + 3A_{2g} + A_{1g} + 4A_{2u} + 4E_g + 6E_u$ at the zone center for the

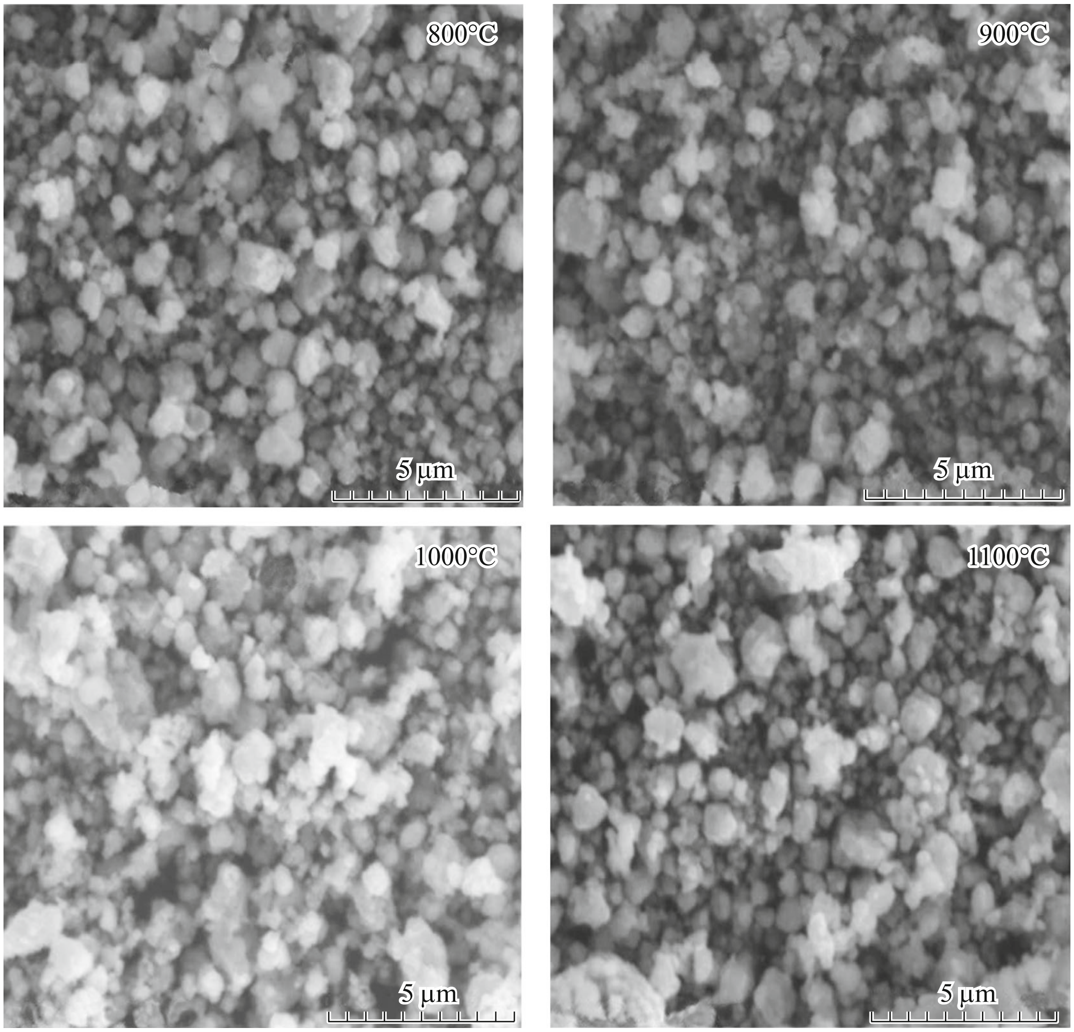

Fig. 2. SEM micrographs of $La_{0.67}Sr_{0.33}Mn_{1-x}Fe_xO_3$ ($x = 0.35$) prepared samples at various temperatures ($T = 800$ to 1100°C).

D_{3d}^6, $Z = 2$ rhombohedral structures. Among these, $A_{1g} + 4E_g$ are Raman active modes while $3A_{2u} + 5E_u$ are infrared active ones and the remaining $2A_{1u} + 3A_{2g}$ are silent modes. Two modes ($1A_{1g} + 1E_g$) correspond to rotational or tilt stretching mode while one E_g mode corresponds to the bending mode. Other two E_g modes are antistretching of the MnO_6 octahedra and vibration of A ions [57, 58]. The A_{1g} modes involve the vibrations of the oxygen ions only in the C_2 sites while E_g modes arise both from oxygen and La (Sr) ions vibrations [59]. The low frequency peak at 221 cm^{-1} and other peak at 409 cm^{-1} are assigned to A_{1g} and E_g modes respectively [5, 57, 60, 61]. The A_{1g} mode arising due to the rotation of the oxygen octahedral agrees well with the shell model calculation of the isostructural $R\bar{3}c$ $LaMnO_3$ [62]. The shell model calculation predicts the A_{1g} mode at 220 cm^{-1} while E_g modes appear at 294, 404, and 681 cm^{-1}. Our results are consistent with the shell model calculation as well as from [56] which shows that the rhombohedral structure has the A_{1g} mode in the range of 190–220 cm^{-1}. Furthermore, the vibration pattern of this mode has the shape of the rhombohedral distortion [62].

Table 3 clearly shows that the A_{1g} modes in our spectra harden going from 300 to 80 K which is in accordance with [56, 63]. The frequency of Raman active modes for LSMFO samples calcined at different temperatures are presented in Table 3. This table clearly exhibits a significant dependence of the Raman active phonon modes on calcination temperature. Our room temperature spectra presented in Fig. 4a clearly shows that the A_{1g} mode is red shifted with calcination temperature, while the low temperature spectra do not show any significant shift though the both 80 and 300 K spectra have difference of about 4 to 13 cm^{-1}. The difference is a maximum in the peak position for both spectra in the case of 1100°C calcined sample. All

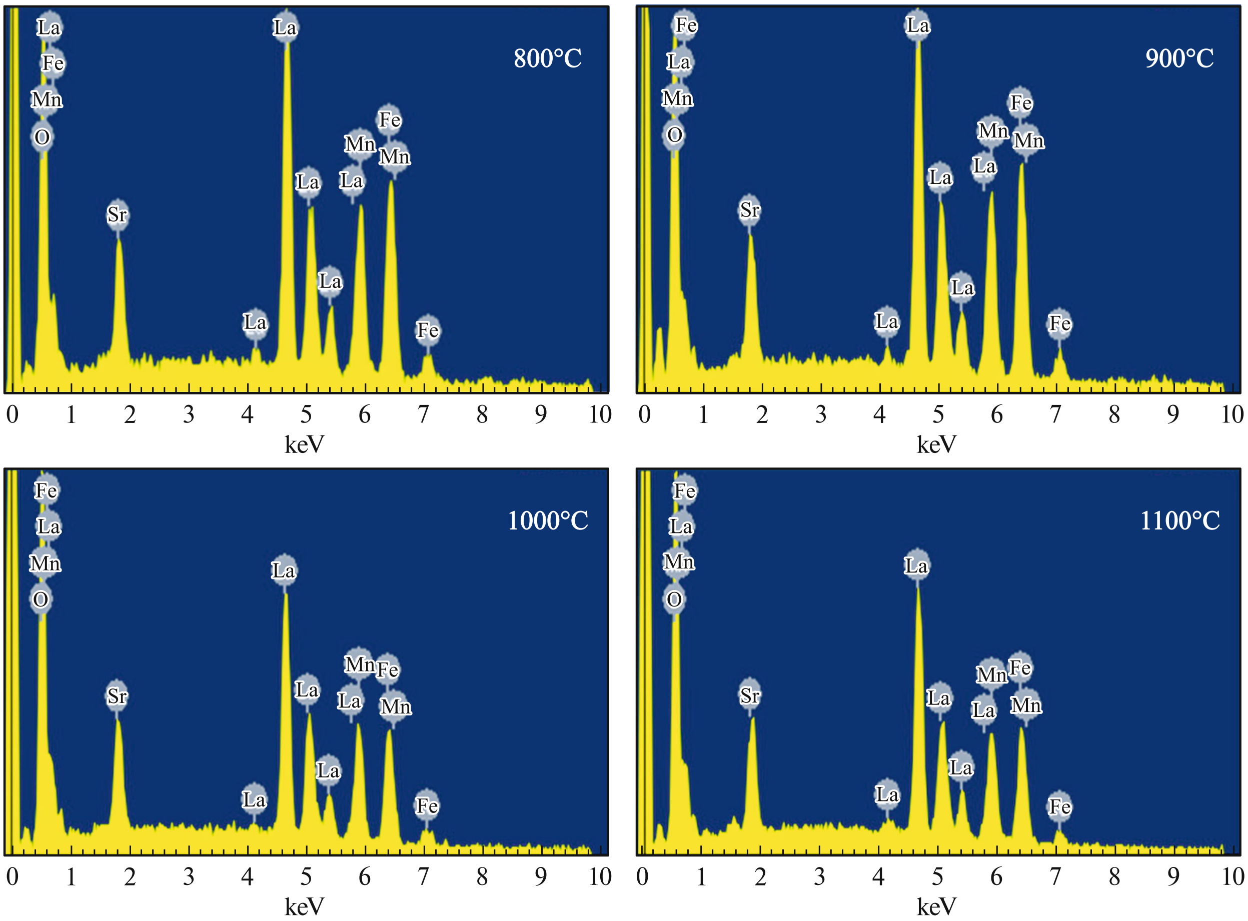

Fig. 3. Elemental analysis using EDAX spectra of Fe doped LSMO ($x = 0.35$) at $T = 800$ to 1100°C.

E_g modes are red shifted with calcination temperature. In both figures, it is clearly seen that the low frequency modes disappear above 1000°C temperature. The highest E_g mode which is broader in the 80 K spectra for all calcination temperatures turns sharper with increasing intensity indicating small or missing rhombohedral distortion consistent with the results of XRD. The E_g mode (414 cm^{-1}) for lowest calcination temperature does not only get shifted towards the higher wave numbers but also becomes sharper indicating proper formation of samples. The highest two E_g modes harden with increasing calcination temperature. The broadening of the peaks can be attributed to the distortion of the oxygen sublattice [55]. The decreases, in the broadening of the two highest E_g modes indicate a decrease in JT effect and distortions of the oxygen sublattice [55]. The broader peak ≈683 cm^{-1} arising due to scattering induced by orthorhombic distortions [61] shifts towards a higher wave number. Figure 5 presents the calcination temperature

Table 2. The comparative data of the composition obtained from EDAX spectra

Sample	Atomic weight (%) $x = 0.35$ (800°C)	Atomic weight (%) (900°C)	Atomic weight (%)(1000°C)	Atomic weight (%) (1100°C)
La	13.27	12.55	15.76	16.15
Sr	3.61	3.58	3.67	3.86
Mn	9.66	10.07	12.27	11.61
Fe	12.74	13.22	14.36	14.33
O	60.73	60.58	53.94	54.04

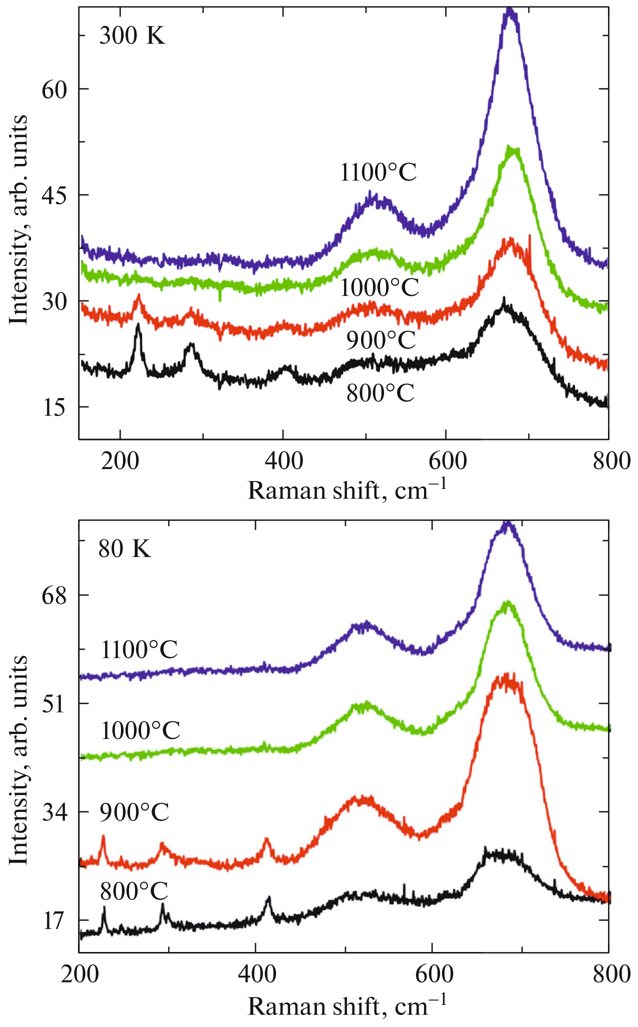

Fig. 4. Vibrational properties using Raman spectra of $La_{0.67}Sr_{0.33}Mn_{1-x}Fe_xO_3$ ($x = 0.35$) prepared samples.

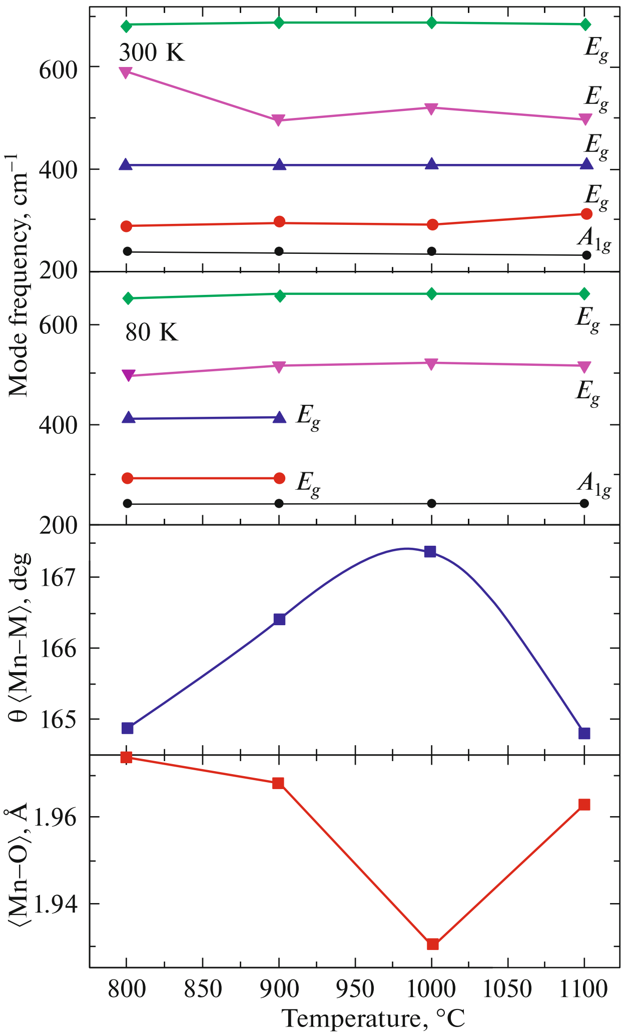

Fig. 5. Calcination temperature dependencies of Raman active mode frequencies, Mn–O–Mn angles and Mn–O bond lengths.

dependent frequency of A_{1g} and E_g modes together with the Mn–O–Mn bond angle and the Mn–O bond length. This figure clearly shows almost same dependency of these quantities on calcination temperature.

4. CONCLUSIONS

In summary, we have investigated the structural, morphological and vibrational properties of $La_{0.67}Sr_{0.33}Mn_{1-x}Fe_xO_3$ ($x = 0.35$) prepared using ball milling method. Our studies show that the structural,

Table 3. Raman mode frequencies of the Fe doped LSMO at room temperature as well as at low temperature (80 K)

Raman modes	$La_{0.67}Sr_{0.3}Mn_{0.65}Fe_{35}O_3$ at 300 K				80 K			
	$x = 0.35$ (800°C)	(900°C)	(1000°C)	(1100°C)	(800°C)	(900°C)	(1000°C)	(1100°C)
A_{1g}	221	221	219	217	226	227	227	228
E_g	286	294	288	285	292	294	–	–
E_g	409	404	415	408	414	411	410	414
E_g	675	678	681	677	675	683	684	685

morphological and vibrational properties depend strongly on the calcination temperature. Synthesized samples are refined using the FullProf program and found to be crystallize in the rhombohedral structure with $R\overline{3}c$ space group. Lattice parameters and the unit cell volume decrease with increasing calcination temperature. The crystallite size calculated from Scherrer formula confirms the formation of nanosize polycrystalline samples of LSMFO. The average crystallite size increases with the increase calcination temperature. The effect of increasing temperature on morphological properties is studied using scanning electron microscope which shows that the particles are agglomerated and the grain size ranges between 240–400 nm. The porosity is shown to decrease with increasing temperature. The presence of all the corresponding elements by EDAX for all prepared samples is confirmed and no additional impurity peak is detected. Raman spectra of LSMFO exhibit a significant change in the peak positions and intensity the Raman active modes due to the temperature effect. The decrease in the broadening of the highest E_g peaks indicates a decrease in the Jahn–Teller distortion. The A_{1g} mode which has the vibrational pattern of rhombohedral distortion hardens while going from 300 to 80 K and softens with increasing calcination temperature. The decrease in the broadening of E_g modes shows reduction in the JT distortion. There is a shift in the peak positions due to increased temperature indicating a change in the MnO_6 octahedron.

FUNDING

Financial assistance from the UGC, New Delhi is highly acknowledged. One of us NA is thankful to the UGC for the award of UGC–BSR Fellowship.

ACKNOWLEDGMENTS

We are thankful to UGC–DAE–CSR Indore for providing the Raman facility. We are also thankful to Geology department of the M.S. University of Baroda for providing the SEM facility.

REFERENCES

1. C. N. R. Rao and A. K. Raychaudhuri, *Colossal Magnetoresistance, Charge Ordering and Other Novel Properties of Manganates and Related Materials* (World Scientific, Singapore, 1998).
2. Y. L. Chang, Q. Huang, and C. K. Ong, J. Appl. Phys. **91**, 789 (2002).
3. E. Dagotto, *Nanoscale Phase Separation and Colossal Magnetoresistance* (Springer, New York, 2003).
4. S. Jin, T. H. Tiefel, M. McCormark, R. A. Fastnacht, R. Ramesh, and L. H. Chen, Science (Washington, DC, U. S.) **264**, 413 (1994).
5. M. Talati and P. K. Jha, Phys. Rev. B **74**, 134406 (2006).
6. M. Talati and P. K. Jha, Comput. Mater. Sci. **37**, 64 (2006).
7. Y. Tokura and Y. Tomioka, J. Magn. Magn. Mater. **200**, 1 (1999).
8. X. H. Huang, J. F. Ding, Z. L. Jiang, Y. W. Yin, Q. X. Yu, and X. G. Li, J. Appl. Phys. **106**, 083904 (2009).
9. U. A. Joshi and J. S. Lee, Solid State Phenom. **119**, 275 (2007).
10. T. Tsuchiya, T. Yoshitake, Y. Shimakawa, Y. Kubo, Y. Yamaguchi, T. Manabe, T. Kumagai, and S. Mizuta, Appl. Phys. A **79**, 1537 (2004).
11. A. J. Darbandi, T. Enz, and H. Hahn, Solid State Ionics **180**, 424 (2009).
12. M. Izumi, Y. Murakami, Y. Konishi, T. Manako, M. Kawasaki, and Y. Tokura, Phys. Rev. B **60**, 1211 (1999).
13. V. S. Reddy Channu, R. Holze, H. Edwin, and H. Walker, New J. Glass Ceram. **3**, 29 (2013).
14. W. Chérif, M. Ellouze, A. F. Lehlooh, S. H. Mahmood, and F. Elhalouani, Hyperfine Interact. **211**, 153 (2012).
15. V. Kulkarni, K. R. Priolkar, P. R. Sarode, R. Rawat, A. Banerjee, and S. Emura, J. Phys.: Condens. Matter. **20**, 075203 (2008).
16. L. Joshi and S. Keshri, Measurement **44**, 938 (2011).
17. G. C. Milward, M. J. Calderon, and P. B. Littlewood, Nature (London, U.K.) **433**, 607 (2005).
18. O. Cepas, H. R. Krishnamurthy, and T. V. Ramakrishnan, Phys. Rev. Lett. **94**, 247207 (2005).
19. T. M. Tank, D. Bhargava, V. Sridharan, S. S. Samatham, V. Ganesan, and S. P. Sanyal, Adv. Mater. Res. **1047**, 123 (2014).
20. C. N. R. Rao, A. R. Raju, V. Ponnambalam, S. Parashar, and N. Kumar, Phys. Rev. B **61**, 594 (2000).
21. J. Gutiérrez, F. J. Bermejo, J. M. Barandiarán, S. P. Cottrell, P. Romano, C. Mondelli, J. R. Stewart, L. F. Barquían, and A. Peña, Phys. Rev. B **73**, 054433 (2006).
22. C. Zener, Phys. Rev. **82**, 403 (1951).
23. J. Gutierrez, A. Peña, J. M. Barandiaran, J. L. Pizarro, T. Hernandez, L. Lezama, M. Insausti, and T. Rojo, Phys. Rev. B **61**, 9028 (2000).
24. D. Acharya, A. Bhargav, T. M. Tank, and S. P. Sanyal, AIP Conf. Proc. **1728**, 020043 (2016).
25. K. M. Krishnan and H. L. Lu, Phys. Rev. B **60**, 14793 (1999).
26. L. Seethalakshmi, V. Sridharan, D. V. Natarajan, R. Rawat, S. Chandra, V. S. Sastry, and T. S. Radhakrishnan, J. Magn. Magn. Mater. **279**, 41 (2004).
27. B. Raveau, Phil. Trans. R. Soc. A **366**, 83 (2008).
28. Y. Sun, X. Xu, and Y. Zhang, Phys. Rev. B **63**, 054404 (2000).
29. D. Bhargava, T. M. Tank, and A. Bodhaye, Trans. Indian Inst. Met. **65**, 443 (2012).
30. C. Hao, B. Zhao, G. Kuang, and Y. Sun, Phys. Status Solidi B **248**, 2921 (2011).
31. M. S. Kim, J. B. Yang, J. Medvedeva, W. B. Yelon, P. E. Parris, and W. J. James, J. Phys.: Condens. Matter **20**, 255228 (2008).

32. K. S. Syed Ali, R. Saravanana, A. V. Pashchenko, and V. P. Pashchenko, J. Alloys Compd. **501**, 307 (2010).
33. A. G. Mostafa, E. K. Abdel-Khalek, W. M. Daoush, and S. F. Moustfa, J. Magn. Magn. Mater. **320**, 3356 (2008).
34. K. H. Ahn, X. W. Wu, K. Liu, and C. L. Chien, Phys. Rev. B **54**, 15299 (1996).
35. J. W. Cai, C. Wang, B. G. Shen, J. G. Zhao, and W. S. Zhan, Appl. Phys. Lett. **71**, 1727 (1997).
36. J.-M. Liu, T. Yu, Q. Huang, J. Li, Z. X. Shen, and C. K. Ong, J. Phys.: Condens. Matter **14**, L141 (2002).
37. N. Kumar, H. Kishan, A. Rao, and V. P. S. Awana, J. Alloys Compd. **502**, 283 (2010).
38. G. Huo, Q. Yang, F. Dong, and D. Song, J. Alloys Compd. **464**, 42 (2008).
39. G. Campillo, A. Gil, O. Arnache, J. J. Beltran, J. Osorio, and G. Sierra, J. Phys.: Conf. Ser. **466**, 012022 (2013).
40. D. Grossin and J. G. Noudem, Solid State Sci. **6**, 939 (2004).
41. M. Gupta, P. Yadav, W. Khan, A. Azam, A. H. Naqvi, and R. K. Kotnala, Adv. Mater. Lett. **3**, 220 (2012).
42. R. Carjaval, in Proceedings of the 15th Congress of the International Union of Crystallography, and Satellite Meeting on Powder Diffraction, Toulouse, p. 127 (1990).
43. M. Khlifi, M. Bejara, O. El Sadekb, E. Dhahria, M. A. Ahmed, and E. K. Hlil, J. Alloys Compd. **509**, 7410 (2011).
44. D. Fatnassi, J. L. Rehspringer, E. K. Hlil, D. Niznansky, M. Ellouze, and F. Elhalouani, J. Supercond. Nov. Magn. **28**, 2401 (2015).
45. N. D. Lipham, G. M. Tsoi, and L. E. Wenger, IEEE Trans. Magn. **43**, 3088 (2007).
46. N. Astik, P. K. Jha, and A. Pratap, J. Electron. Mater. **47**, 1937 (2018).
47. A. Gaur and G. D. Varma, J. Phys.: Condens. Matter **18**, 8837 (2006).
48. M. M. Xavier, F. A. O. Cabral, A. de Uacute, J. H. Jo, C. Chesman, and T. Dumelow, Phys. Rev. B **63**, 012408 (2000).
49. W. X. Xianyu, B. H. Li, Z. N. Qian, and H. M. Jin, J. Appl. Phys. **86**, 5164 (1999).
50. Y. Sun, W. Tong, X. J. Xu, and Y. H. Zhang, J, Appl. Phys. Lett. **78**, 643 (2001).
51. C. H. Wei, L. K. Pah, A. H. Shaari, C. S. Kien, A. Gan, N. S. Wei, and W. J. Kuen, Solid State Sci. Technol. **20**, 148 (2012).
52. X. Guo Cao and S. Ping Jiang, J. Mater. Chem. A **2**, 20739 (2014).
53. P. K. Siwach, U. K. Goutam, P. Srivastava, H. K. Singh, R. S. Tiwari, and O. N. Srivastava, J. Phys. D **39**, 14 (2006).
54. Z. F. Zi, Y. P. Sun, X. B. Zhu, Z. R. Yang, J. M. Dai, and W. H. Song, J. Magn. Magn. Mater. **321**, 2378 (2009).
55. N. D. Thorat, K. P. Shinde, S. H. Pawar, K. C. Barick, C. A. Betty, and R. S. Ningthoujam, RSC Adv. 41, 3060 (2012).
56. A. Dubroka, J. Humlíęk, M. V. Abrashev, Z. V. Popović, F. Sapíña, and A. Cantarero, Phys. Rev. B **73**, 224401 (2006).
57. L. Martin-Carron, A. de Andres, M. J. Martinez-Lope, M. T. Casais, and J. A. Alonso, Phys. Rev. B **66**, 174303 (2002).
58. P. T. Phong, S. J. Jang, B. T. Huy, Y.-I. Lee, and I. J. Lee, J. Mater. Sci. Mater. Electron. **24**, 2292 (2013).
59. D. L. Rousseau, R. P. Bauman, and S. P. S. Porto, J. Raman Spectrosc. **10**, 253 (1981).
60. B. C. Behera, A. V. Ravindra, P. Padhan, and W. Prellier, Appl. Phys. Lett. **104**, 092406 (2014).
61. E. Granado, N. O. Moreno, A. Garcia, J. A. Sanjurjo, C. Rettori, I. Torriani, S. B. Oseroff, J. J. Neumeier, K. J. McClellan, S. W. Cheong, and Y. Tokura, Phys. Rev. B **58**, 11435 (1998).
62. M. V. Abrashev, A. P. Litvinchuk, M. N. Iliev, R. L. Meng, V. N. Popov, V. G. Ivanov, R. A. Chakalov, and C. Thomsen, Phys. Rev. B **59**, 4146 (1999).
63. L. Martín-Carrón and A. de Andrés, Eur. Phys. J. B **22**, 11 (2001).

Accepted Manuscript

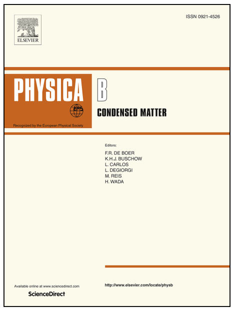

Influence of Fe substitution on structure and Raman spectra of $La_{0.67}Sr_{0.33}MnO_3$: Experimental and density functional studies

Nidhi M. Astik, Himadri Soni, Prafulla K. Jha, Vasant Sathe

PII: S0921-4526(18)30304-1

DOI: 10.1016/j.physb.2018.04.038

Reference: PHYSB 310854

To appear in: *Physica B: Physics of Condensed Matter*

Received Date: 7 November 2017

Revised Date: 15 February 2018

Accepted Date: 24 April 2018

Please cite this article as: N.M. Astik, H. Soni, P.K. Jha, V. Sathe, Influence of Fe substitution on structure and Raman spectra of $La_{0.67}Sr_{0.33}MnO_3$: Experimental and density functional studies, *Physica B: Physics of Condensed Matter* (2018), doi: 10.1016/j.physb.2018.04.038.

Influence of Fe Substitution on Structure and Raman Spectra of $La_{0.67}Sr_{0.33}MnO_3$: Experimental and Density Functional Studies

Nidhi M Astik[1], Himadri Soni[2], Prafulla K. Jha[1] and Vasant Sathe[3]

[1]Departmen of Physics, The M. S. University of Baroda, Vadodara,390002,Gujarat, India.
[2] Lehrstuhl fur TheoretischeChemie, Friedrich-Alexander Universit € at Erlangen-N € urnberg, € Egerlandstraße 3, 91058 Erlangen, Germany
[3]UGC-DAE Consortium for scientific Research, University Campus, Khandwa Road, Indore,452017, India.

ABSTRACT

We present experimental and theoretical studies on the effect of Fe doping at Mn site, on the structural, morphological, electronic and vibrational properties of $La_{0.67}Sr_{0.3}MnO_3$ nanoparticle. The samples of $La_{0.67}Sr_{0.3}MnO_3$ and $La_{0.67}Sr_{0.33}Mn_{1-x}Fe_xO_3$ (x=0.15, 0.25 and 0.35) have been prepared by ball milling route. The phase purity of these samples has been confirmed using X-ray diffraction, while compositional analysis is done using EDAX. The morphological analysis done using scanning microscope indicates the agglomeration. The vibrational analysis which is done using Raman scattering and density functional theory (DFT) calculations show a substantial shift in A_{1g} and E_g modes with Fe doping. The E_g modes become broader with Fe doping.The UV –visible spectra were measured in the energy range of 1 – 5 eV and compared with DFT results. The spin polarized density functional calculations show an increase in density of states at Fermi level due to MnO_6octahedra modification and significant magnetism on Fe doping. The total magnetic moment is found from 16 to 17 μ_B for considered concentration. The effective mass of carriers is also calculated and found increasing with increasing concentration.

Keywords

Manganites, Ball milling, Structure, Morphology, Raman Spectroscopy, Density Functional Theory

[*]Corresponding author: Prof. Prafulla. K. Jha

Email: prafullaj@yahoo.com

Telephone: +91-265-2795339; Fax: +91-265-2792277

1. Introduction

Extensive studies probing the properties of mixed valent manganites $Ln_{1-x}A_xMnO_3$ (A=Ca, Sr, Ba) with perovskite structure have been carried out for almost six decades, due to their exciting physical and structural properties arising from the coupling of spin, lattice charge and orbital degree of freedom [1]. These properties are found quite sensitive to the type and strength of lattice distortion [2, 3], the filling of one-electron level and its width [4] and internal strain [5]. Thus manganites offer a degree of chemical and physical flexibility to control and manipulate their structural, electronic and magnetic states. The colossal magnetoresistance (CMR) has been a source of great interest for these manganites in recent past due to their potential applications in spintronics, magnetic storage system, magnetic field sensors, solid state, refrigerators and infrared devices [6-9].In addition, the perovskites offer diverse physical properties depending on the doping concentration ‘x’ and preparation route [10]. Many of these properties are explained by the double exchange mechanism (DE) arising from the interaction between Mn^{4+} - Mn^{3+} ion pairs and Jahn – Teller distortion of Mn^{3+} ion resulting into the electron - phonon coupling and polaron effects [11,12]. It is well known that the interaction between electrons and lattice distortion play an important role in physics of these compounds. The Mn e_g electrons which are responsible for the rich variety of attractive properties, couple to lattice through Jahn-Teller effects [13]. However, in the metallic phase, the conduction band consists of 3d e_g states hybridizes strongly with the O2p states with localized t_{2g} electrons. The multiplicity of the crystallographic and magnetic phase in the doped crystals suggests that the ground state of these systems depend upon a subtle interplay between their microscopic electrical, magnetic and lattice properties and excitations [14, 15]. The double exchange mechanism qualitatively explained the ferromagnetic interactions and the observed metallic behaviour below the Curie temperature T_C, but was inadequate to explain the observed resistivity above the transition temperature and even most importantly the observation of CMR in Fe doped $LaSrMnO_3$ (LSMO) [16]. Conversely, the more recent spin-polarized density functional theory (DFT) calculation of the density of states (DOS) provides several clues to the underlying processes involved in the CMR phenomena explained the observation of CMR in stoichiometric phases [17].

There exist several methods to prepare these materials including co-precipitation or precipitation, sol – gel and ball milling [18, 19]. The mechanical ball milling method is one of the powerful methods in powder metallurgy because of the high flexibility and ability to produce a wide range of materials [20]. It is an efficient method to prepare many unique materials, such as nanostructure crystalline amorphous alloys and nano oxides particularly from the powder oxide [21, 22]. It is found that the substitution of lanthanum or manganese by another ion influences the properties of manganites. While the substitution at A site i.e. lanthanum or manganese by another ion modifies interactions in the La-O and Mn-O networks. The substitution of other transition elements at the Mn (B) site produces changes in the average concentration and shift in the positions of the e_g and t_g sub bands [23,24]. The Fe doping in this context has received considerable attention due to the large extent to which it can replace Mn and has a magnetic nature [25 - 27]. Further, the Fe substitution fine tunes the DE mechanism by breaking the DE chain [28-29]. The increase in Fe concentration shows remarkably decrease in strength of DE and T_C [30].

In the present paper, we report on structural, morphological and vibrational properties of the polycrystalline Fe doped LSMO samples prepared by the mechanical ball milling synthesis method and state of art first principles calculations based on density functional theory. For experimental structural, morphological, elemental and vibrational characterizations, we use X-ray diffraction (XRD), Scanning electron microscope (SEM), and energy dispersive x-ray spectroscopy (EDAX) and Raman spectroscopy respectively. These results are then compared with the DFT results obtained in the present study.

2. Materials and Method

2.1. Preparation of samples

In this work, pure phase of ferromagnetic manganite $La_{0.67}Sr_{0.33}Mn_{1-x}Fe_xO_3$(LSMFO) was obtained by solid state reaction method subjected to the conventional ball-milling method. The synthesis procedure was as follows, high purity precursors MnO_2, La_2O_3, SrO, and Fe_2O_3 in the appropriate proportions according to the following reactions:

$$0.335La_2O_3 + 0.33SrO + x/2\ Fe_2O_3 + (1-x)\ MnO_2 \rightarrow La_{0.67}Sr_{0.33}Mn_{1-x}Fe_xO_3 + \delta\ Co_2$$

Polycrystalline samples of $La_{0.67}Sr_{0.33}Mn_{1-x}Fe_xO_3$ were synthesized by relative milling method. The powder milling process was performed with commercial FRITISCH planetary micro mill PULVERISETTE – 5. This mixture of high purity powders was carried out at room temperature and under normal atmosphere. This planetary ball milling with stainless still balls was used for this purpose with the ball to powder ratio of 10:1 and rotation speed of 250 rpm [31]. The final product was subjected to the heating treatment at 800°C for 7 hours with the rates of heating rate of 5°C/min.

All the powder samples were characterized for structural properties by X-ray diffraction at room temperature using PANalytical X'Pert Pro diffractometer with CuK_α radiation (λ = 1.5406 Å)The composition and surface morphology of resulting products were investigated using JEOL JMS-5610LV scanning electron microscope and molar ratio of elements in sample was evaluated by Oxford INCA Energy Dispersive analysis of x-ray (EDAX).The vibrational Raman spectra were measured by JOBIN YVON HORIBA-HR800.The UV-vis absorption spectra in the range of 200-800 nm spectra range were recorded with SHIMADZU, UV-2450 spectrometer.

2.2. Computational Details

Ab-initio calculations in the present study for $La_{0.67}Sr_{0.33}Mn_{1-x}Fe_xO_3$(x=0.15, 0.25 and 0.35) have been performed within the local density approximation (LDA) and local spin density approximation (LSDA) to the exchange correlation potential within the framework of density functional theory using the Vienna ab-initio simulation package (VASP) [32]. We have used a computational unit cell of LSMFO to simulate the rhombohedral R -3 c within the ferromagnetic (FM) ordering. Convergence tests on the energy cut off is 500 eV. The Brillouin zone sampling was performed according to Monkhorst-pack method [33] using the 10 × 10 × 10 grid and 12 × 12 × 12K-points, whereas the density of states was calculated using the tetrahedron method [34] to generate the K-points within the irreducible wedge of the Brillouin zone. For structural optimization procedureeach lattice parameter (a, b, and c as well as the corresponding angles between them) and all internal structure degree of freedom (all atomic positions) have been fully relaxed. This ensures the proper optimization of the unit cell with zero pressure [35-37]. This complete geometrical optimization allows us to treat the structural path of the rhombohedral phase [38]. The starting crystal parameters of the $LaSrMnFeO_3$ have been taken from our present XRD data of corresponding samples.

3. Results and Discussions

3.1. Structure and Morphology

Figs.1 (a) & (b) present the x-ray diffraction pattern collected by step scanning over the angular range $20^o \leq 2\theta \leq 80^o$ at a step size of 0.02 for as prepared $La_{0.67}Sr_{0.33}Mn_{1-x}Fe_xO_3$with nominal composition (x=0.15, 0.25 and 0.35) at room temperature.

The diffraction profiles have been refined successfully using the Rietveld refinement using FULLPROOF program method with rhombohedral R-3 c lattice structure. High intensity of diffraction peak for LSMFO perovskite phase at high sintering temperature (800^{o}C) is the clear indication of better sample crystallinity [39, 40]. The XRD profiles of the samples in Fig.1 (a), (b) and (c) reflect slight decrease in the width of Fe ion suggesting the formation of polycrystalline samples of larger crystallite size. The lattice and related parameters of the samples obtained so have been presented in Table 1 together with the DFT data. It is to be noted that the LSDA calculations give a good agreement with experimentally obtained structural and equilibrium parameters. However, the inclusion of correlation effects like Hubbard like potential acting on the Mn 3d sides overestimate the lattice constants by 0.7 to 2.2 %. For our calculation we considered the value of U as 7.0 eV [41].The table shows that the lattice parameters increase with the increasing doping amount. The X-ray line widths are used to estimate the average particle size through the classical Scherrer formula$D = k\lambda/(\beta \cos 2\theta)$,where D is the particle size, k is the constant (0.9), b is the full width at the half maximum of a peak, and λ is the wavelength of the x-ray. The Table 1 also presents the calculated average particle size and goodness fit of the samples determined from the Scherrer formula and Rietveld refinement respectively. The enhancement in crystallite size is observed in the sample with Fe concentration of x= 0.15 in comparison to x=0.25 and x=0.35. A reasonably good agreement is observed between the experimentally observed and DFT calculated data for optimized structures.

We note a slight increase in the lattice parameters and unit cell volume with the augmentation of iron content. This can be attributed to the direct replacement of Mn^{3+} ion by identical sized Fe^{3+} which results into the polaron that can affect the Mn-O bond length and Mn-O-Mn angle in $La_{0.67}Sr_{0.33}Mn_{1-x}Fe_xO_3$ compounds [42, 43].

The detailed morphology and composition of the prepared samples with Fe concentration of 0.15, 0.25 and 0.35 have been recorded using scanning electron microscope (SEM) and energy dispersive analysis of x-ray (EDAX) respectively. The SEM images presented in Figs. 2 (a) & (b) &(c) reveal that the prepared samples are inherently uniform and have an agglomeration with undefined shape like morphology with undisturbed pores. It is also clear from the SEM micrographs that the particles are highly agglomerated with irregular boundaries due to high homogeneity during synthesis at different doping concentration [44].

The EDAX spectrum which is used for quantitative elemental analysis of the composition of the LSMFO samples prepared by solid state reaction presented in Fig.3 confirms in proper composition in the case of both samples. However, it should be noted that the EDAX analysis presented in Table 2 is a semiquantitative analysis and it is not sensitive for light elements such as oxygen. The spectra indicate that the both samples are consistent with their elemental signals and expected stoichiometry. The corresponding peaks in the EDAX spectra are due to La, Sr, Mn, Fe and O elements. No additional impurity peak is observed which is confirms that the prepared samples are pure in nature [45]. The atomic weight ratio of (La, Sr):(Mn, Fe) = 1.0 suggests stoichiometric nature of both samples.

3.2. Vibrational Analysis

The present samples are in rhombohedral structures (R-3c), with space group D^6_{3d}, Z=2 which can be obtained from the simple cubic perovskite by the rotation of the adjacent MnO_2octahedra in the opposite direction around the $[111]_c$ cubic direction [46]. The theoretical and experimental descriptions of the Raman spectra have been briefed in Refs. [35-36]. There are five Raman (A_{1g} +4E_g) are eight infrared (3A_{2u} + 5E_u) active modes. Fig. 4 presents the room and low (80K) temperature Raman spectra of Fe doped $La_{0.67}Sr_{0.3}MnO_3$compounds annealed at 800°C for 7 hours collected using 632.8 nm excitation wavelengths in the frequency interval of 200-800 cm^{-1}.

The A_{1g} modes only involve the vibrations of the oxygen ions in the C_2 sites while E_g modes arise both from oxygen and La (Sr) ions [47] ions vibrations. Based on the Refs. [35-37, 48] low frequency peak at$A_1$is assigned to A_{1g} symmetry while the peak $A_3$is assigned to E_g symmetry. There is clear shift for both of these modes toward lower wave number with the increase in doping content of Fe. The two broader peaks ≈ 530 (A_4) and ≈ 670cm^{-1} (A_5) arising due to scattering induced by orthorhombic distortions [49] shift to higher wave number. These are the characteristic modes of manganites arising from the Jahn-Teller distortions [50 - 53]. The broadening increases for both modes with Fe content indicating that the Jahn-Teller distortion increases with Fe concentration. Furthermore, the frequency shifts with doping results from the induced ions involving the motion of oxygen cages and an effective octahedral rotation [54]. There is an increase in compression arising from the stress due to the Fe doping at B site and Mn-O bond length change [52]. There are two more broad peaks A_2 and A_4 around 500 cm^{-1} and 290 cm^{-1} respectively which show reverse characteristics with concentration. While A2 band softens the A4 band hardens. However, the peak position for x=0 is quite prominent in the case of room temperature spectra. Now let us focus on 80 K spectra. The broad bands are caused by distortions of the oxygen sublattice [46]. The E_g (A_3) and A_{1g} (A_1) modes which soften with the concentration harden with decreasing temperature. These are consistent with the Dubroka et al [46] for other heavier ion doping at B-sites. We have also performed the first principles calculation of Raman mode frequency of LSMO sample annealed at 800^{o}C with Fe doping of 0.15 and x= 0.25 and x=0.35and presented them in Table 3together with room temperature experimental Raman data. There is a reasonably good agreement between both.

3.3 Electronic density of states

To understand the origin of the metallic ferromagnetism in the doped manganites it is necessary to understand their electronic structure. For this, first principles calculation based on density functional theory within the local spin density approximation (LSDA) implemented in VASP program is performed [32].The electronic band structure together with the total density of states for three concentrations (x=0.15, 0.25 and 0.35) of Fe doping in LSMO for both for up and down spins are presented in Fig.5 (a-c) which shows increase in density of states at Fermi level (E_F). We have obtained the effective mass from the band structure calculations using expression

$m^* = \frac{\hbar^2}{(2d)} \times m_e$. We observed that the effective mass of carriers m^*/m_e is 3.53, 3.98 and 4.95 for x=0.15, 0.25 and 0.35 respectively [55, 56]. The effective mass increases with concentration. It is clarified that the deformation of $LaSrMnFeO_3$ polycrystalline has a significant influence on the band mass but the electronic effect due to the e_{2g} band flattening near the gamma point due to the Fe doping up to 0.35 at % is the main factor for the effective mass increases [56].

The LSDA results give a strong FM interaction without any sign of antiferrromagnetism for these systems. When compared with previous work [54], no significant changes are observed for the Mn-d states with increasing Fe content and only e_g states in the majority-spin channel contribute to the DOS at E_F. We have also calculated the total magnetic moment of the Mn atoms which are surrounded by different cationic environment [57]. We have not listed the contribution from La, Sr and O atoms to the total magnetic moment of the unit cell. The calculated magnetic moment of the unit cell is 16.52, 17.04 and 16.6 μ_B for x=0.15, 0.25 and 0.35 respectively consistent with earlier report [58]. The enhancement of magnetic moments can be attributed to the change of complex interaction between Mn atoms and other atoms mainly the O atoms induced by octahedral rotation and deformation [59]. The average magnetic moment on the Mn atoms slightly increase from 2.49, 2.51 and 2.45 μ_B for x=0.15, 0.25 and 0.35 respectively [60].

3.4 Absorption Spectra

The absorption properties of Fe doped LSMO are measured from the UV-vis spectroscopy and evaluated by absorption coefficient α (ω) defined as:

$$\alpha(\omega) = \sqrt{2}\,(\omega)\left[\sqrt{\varepsilon_1\,(\omega^2) + \varepsilon_2\,(\omega^2)} - \varepsilon_1(\omega)\right]^{1/2} \qquad (1)$$

Where ω is the frequency and ε_1 (ω) and ε_2 (ω) are the real and imaginary parts of the dielectric function, respectively [61]. Figure 6 illustrates the UV-vis absorption spectrum of prepared LSMFO with x=0.15, 0.25 and 0.35 doping concentration together with the DFT calculated spectra (inset). The experimental spectra show peaks at 1.58, 1.60 and 1.65 eV respectively. The absorption peaks shift to the higher value with increasing the doping concentration which is in good agreement with earlier report [62].The slight deviation in the theoretically and experimentally obtained spectra can be attributed to the facts that in real samples there may be some kind of defects present which can significantly influence the absorption properties.

4. Conclusions

In summary, crystallographic, morphological, electronic and vibrational analysis of $La_{0.67}Sr_{0.33}Mn_{1-x}Fe_xO_3$ (x=0.15, 0.25) compounds prepared by ball milled method and ab - initio spin polarized density functional calculations are analysed. The analysis of structure indicates that the compounds are formed in rhombohedral R-3c phase and the lattice parameters show a Fe content dependency. Lattice parameters and unit cell volume increase with Fe dopent. The crystallite size calculated using Scherrer formula confirms the formation of polycrystalline samples of LSMFO. The crystallite size increases with the increase in Fe concentration. The effect of increasing Fe content on morphological properties is studied using scanning electron microscope which shows that the particles are agglomerated. The presence of all the corresponding elements by EDAX for both samples is confirmed and no impurity peak is detected. Raman spectra of LSMO exhibit a significant change due to Fe ions doping. The broadening of the peaks indicates and increases in the Jahn-Teller distortions and compression. There is a shift in the peak positions due to increased doping indicating a change in the MnO_6 octahedron. LSDA calculations reveal that the metallic behaviour without any intimation of antiferrromagnetism for this systems. The total magnetic moments of unit cell for these systems in FM state ranges from 16 to 17 μ_B. The effective mass of carriers increases going from x=0.15 to 0.35. The measured and calculated absorption spectra agree reasonably well.

Acknowledgement

Financially assistance from the UGC, New Delhi is highly acknowledged. One of us NA is thankful to the UGC for the award of UGC-BSR Fellowship. We are thankful to UGC-DAE-CSR Indore for providing the Raman facility. Authors are thankful to head Geology Department and Applied Chemistry Department for providing the SEM and UV- vis facility.

References

1. L. Y. Kuai, Y. Y. Wei, and L. X. Guang, Colossal magnetoresistance in manganites and related prototype devices, Chi. Phys. B 22, (2013) 087502-1-087502-19.
2. J. B. Goodenough, Theory of the Role of Covalence in the Perovskite-Type Manganites [La, M(II)]MnO_3, Phys. Rev.100 (1955) 564-573.
3. E. O. Wollan, W.C. Koehler, Neutron Diffraction Study of the Magnetic Properties of the Series of Perovskite-Type Compounds [(1−x)La, xCa]MnO_3, Phys. Rev. B 100 (1955) 545-563.
4. L. P. Gorkev, Valdimir Z. Kresin, Interaction between the d-Shells in the Transition Metals. II. Ferromagnetic Compounds of Manganese with Perovskite Structure, Phys. Rep. 400 (2004) 149-208.
5. P. Lampen, A. Puri, M. H. Phan, H. Srikanth, Structure, magnetic, and magnetocaloric properties of amorphous and crystalline $La_{0.4}Ca_{0.6}MnO_{3+\delta}$ nanoparticles, J. Alloy. Comp. 512 (2012) 94-99.
6. C. Zener, Interaction between the d-Shells in the Transition Metals. II. Ferromagnetic Compounds of Manganese with Perovskite Structure, Phys. Rev. 82 (1951) 403-405.
7. Y. Tokura, Colossal Magnetoresistive Oxides, Gordon and Breach, New York 2002, pp. 1-53.
8. M. B. Salamon, M. Jaime, The physics of manganites: Structure and transport, Rev. Mod. Phys. 73(2001) 583-608.
9. M. Bibes, A. Bathelemy, Oxide Spintronics, IEEE Trans. Electron devices, 54 (2007)1-18.
10. A. Urishibara, Y. Moritomo, A. Ari, T Asamitsu, G. Kid, Y. Tokura, Insulator-metal transition and giant magnetoresistance in $La_{1-x}Sr_x$ MnO_3, Phys. Rev. B 51 (1995),14103-14109.
11. H. Roder, J. Zang, A. R. Bishop, Lattice Effects in the Colossal-Magnetoresistance Manganites, Phys. Rev. Lett. 76 (1996) 1356-1359.
12. A. J. Millis, B. I. Sharaiman, R. Mueller, Dynamic Jahn-Teller Effect and Colossal Magnetoresistance in $La_{1-x}Sr_x$ MnO_3, Phys. Rev. Lett. 77 (1996) 175-178.
13. A. J. Millis, T. Darling, A. J. Migliori, Quantifying the effects of strain in Colossal magnetoresistance manganites, J. Appl. Phys. 83 (1997)1588-1591.
14. A. J. Millis, P. B. Littele Wood, B. I. Sharaiman, Double exchange alone does not explain the resistivity of $La_{1-x}Sr_x$ MnO_3, Phys. Rev. Lett. 74 (1955) 5144-5147.
15. D. J. Singh, W. E. Pickett, Pseudogaps, Jahn-Teller distortions, and magnetic order in manganite perovskites, Phys. Rev. B 57 (1998) 88-91.
16. M.Cieplak, Localized model for systems with double-exchange coupling, Phys. Rev. B 18 (1978) 3470-3485.
17. Y. Shimakawa, Y. Kubo,T. Manako, Giant magnetoresistance in Ti, Mn, O with the pyrochlore structure, Nature 379 (1996) 53-55.
18. H. Aono, H. Hirazawah, T. Naohara, T. Maehara, H. Kikawa, Y. Watanabe, Synthesis of fine magnetite powder using reverse coprecipitation method and its heating properties by applying AC magnetic field, Mater. Res. Bull. 40 (2005) 1126-1135.
19. M. Venkatesan, S. Nawka, S. Pillai, J. M. D. Coey, Enhanced magnetoresistance in nanocrystalline magnetite, J. Appl. Phys. 93 (2003) 8023-8025.

20. K. D. Machado, J. C. D. Lima, C. E. M. de Campos, T. A. Grandi, A. A. M. Gasperini, Aging of a nanostructured Zn50Se50 alloy produced by mechanical alloying, Solid State Commun. 127 (2003) 477-481.
21. C. Suryanarayan, Mechanical alloying and milling, Prog. Mater. Sci. 46 (2001) 1-184.
22. J. C. D. Lima, V. H. F. dos Santos, T. A. Grandi, Structural study of the Zn-Se System by Ball Milling Technique, Nanostruct. Mater. 11 (1999) 51-57.
23. S. K. Hasanain, M. Nadeem, W. H. Shah, M. J. Akhtar, M. M. Hasan, Effect of iron doping on the transport and magnetic behavior in $La_{0.65}Ca_{0.35}Mn_{1-y}Fe_yO_3$, J. Phys. Condens. Matter 12 (2000) 9007-9017
24. K. Ghosh, S. B. Ogale, R. Ramesh, R. L. Greene, T. Venkatesan, Transition-element doping effects in $La_{0.7}Sr_{0.3}MnO_3$, Phys. Rev. B 59 (1999) 533-537.
25. E. Banks, N. Tashima, Magnetically Ordered Perovskites in the system $La_{1-x}Ca_xFe_{1-x}Mn_xO_3$, J. Appl. Phys. 41 (1970) 1186-1187.
26. G. H. Jonker, Semiconducting properties of mixed crystals with perovskite structure, Physica 20 (1954) 1118-1122.
27. K. H. Ahn, X. W. Liu, K. Liu, C. L. Chien, Magnetic Properties and Colossal Magnetoresistance of $La(Ca)MnO_3$ Materials Doped with Fe, Phys. Rev. B 54 (1996) 15299-15302.
28. J. A. Mydosh, Spin Glasses: An Experimental Introduction Taylor and Francis, London 1993, pp. 1-256.
29. L. F. Barquin, R. G. Calderon, Non linear AC susceptibility behavior of collective dynamics in heterogenerous nanomagnetic systems, J. Phys. Conf. Series 17 (2005) 87-100.
30. H. Ahmed, S. Khan, W. Khan, R. Nongjai, I. Khan, Ferromagnetism and adiabaticto non-adiabatic switching process in $La_{0.33}Sr_{0.63}Mn_{1-x}Fe_xO_3$ $(0<x<0.02)$ manganite, J. Mag. Mag. Mater. 368 (2014) 273-280.
31. N. Astik, S. Patil, P. Bhargava, P. K. Jha, Synthesis and Characteristic of nanocrystalline $La_{0.7}Sr_{0.3}MnO_3$manganites by solid state reaction route, AIP conf. Proceed. 1728 (2016) 020467-1-020467-4.
32. J. He, M.X. Chen, X. Q. Chen, C. Franchini, Structural transitions and transport-half-metallic ferromagnetism in $LaMnO_3$ at elevated pressure, Phys. Rev. B 85 (2012) 195135.
33. H. J. Monkhorst, J. D. Pack, Special points for Brillouin-Zone integration, Phys.Rev. B 13 (1976) 5188-5191.
34. O. Jepsen, O. K. Andersen, The Electronic Structure of h.c.p. Ytterbium, Solid State Commun. 9 (1971) 1763-1767.
35. M. Talati, P. K. Jha, Pressure-dependent phonon properties of $La_{0.7}Sr_{0.3}MnO_3$, Phys. Rev. B 74 (2006) 134406.
36. B. C. Behera, A. V. Ravindra, P. Padhan, W. Prellier, Raman spectra and magnetization of all-ferromagnetic superlattices grown on (110) oriented SrTiO3, Appl. Phys. Lett. 104 (2014) 092406.
37. L. Martin-Carron, A. de Andres, M. J. Martinez-Lope, M. T. Casais, and J. A. Alonso, Raman phonons as a probe of disorder, fluctuations, and local structure in doped and undoped orthorhombic and rhombohedralmanganites, Phys. Rev. B 66, 174303 ~2002.

38. H. Jiangang, M. X. Chen, X. Q. Chen, C. Franchini, Structural transitions and transport-half-metallic ferromagnetism in $LaMnO_3$ at elevated pressure, Phys. Rev. B 85 (2012) 195135-1-195135-7.
39. P. Dey, T. K. Nath, Effect of grain size modulation on the magneto- and electronic-transport properties of $La_{0.7}Ca_{0.3}MnO_3$ nanoparticles: The role of spin-polarized tunneling at the enhanced grain surface, Phys. Rev. B 73 (2006) 214425-1-214425-14.
40. V. Shelke, A. Das, I. Dhiman, R. Yadav, S. Khatarkar, A. Anshul, R. K. Singh, Structural, electrical, magnetic and microstructural behavior of the $La_{0.7}Sr_{0.3-x}Hg_xMnO_3$ ($0 \leq x \leq 0.3$) system, J. Phys. Conden. Mater. 20 (2008) 1-9.
41. M. S. Kim, J. B. Yang, J. Medvedeva, W. B. Yelon, P. E. Parris,W. J. James, Electronic Structure of $La_{0.7}Sr_{0.3}Mn_{1-x}Cu_xO_3$ ($0.0 \leq x \leq 0.30$), J. Phys.: Condens. Matter 20 (2008) 255228.
42. K. H. Ahn, X. W. Wu, K. Liu, C. L. Chien, Effects of Fe doping in the colossal magnetoresistive $La_{1-x}Ca_xMnO_3$, J. Appl. Phys. 81 (1997) 5505-5507.
43. L. Joshi, S. Keshri, Magneto-transport properties of Fe doped LSMO manganites, Measurement 44 (2011) 938-945.
44. K. P. Shinde, S. S. Pawar, P. M. Shirage, S. H. Pawar, Studies on morphological and magnetic properties of $La_{1-x}Sr_xMnO_3$, Appl. Sur. Sci. 258 (2012) 7417-7420.
45. N. D. Thorat, K. P. Shinde, S. H. Pawar, K. C. Barick, C. A. Betty, R. S. Ningthoujam, Polyvinyl alchohol: an efficient fuel for synthesis of superparamagnetic LSMO nanoparticles for biomedical application, RSC Adv. 41 (2012) 3060-3071.
46. A. Dubroka, J. Humlicek, M. V. Abrashev, Z. V. Popovic, F. Sapina, A. Cantarero, Raman and infrared studies of $La_{1-y}Sr_yMn_{1-x}M_xO_3$ (M=Cr, Co, Cu, Zn, Sc, or Ga): Oxygen disorder and local vibrational modes, Phys. Rev. B 73 (2006) 224401-1 -224401-10.
47. D. L. Rousseau, R. P. Bauman, S. P. S. Porto, Normal mode determination in crystals, J. Raman Spectroscopy, 10 (1981) 253-290.
48. E.Granado, N. O. Moreno, A. Garcia, J. A. Sanjurjo, C. Rettori, I. Torriani, S. B. Oseroff, J. J. Neumeier, K. J. McClellan, S-W. Cheong, Y. Tokura, Phonon Raman scattering in $R_{1-x}A_xMnO_{3+\delta}$ (R=La, PR; A= Ca, Sr), Phys. Rev. B 58 (1998) 11435-11440.
49. A. E. Pantoja, H. J. Trodahl, A. Fainstein, R. G. Pregliasco, R. G. Buckely, G. Balakrishnan, M. R. Lees, D. Mck. Paul. O (Mn) vibrational bands in dounle-layered manganites: First and second order Raman scattering, Phys. Rev. B 63 (2001) 132406-1-132405-4.
50. S. Yoon, H. L. Liu, G. Schollerer, S. L. Cooper, P. D. Han, D. A. Payne, S-W. Cheong, Z. Fisk, Raman and optical spectroscopic studies of small –to-large polaron crossover in the perovskite manganese oxides, Phys. Rev. B 58 (1998) 2795-2801.
51. A. Congeduti, P. Postorino, E. Caramangno, M. Nardone, A. Kumar, D. D. Sarma, Anamalous High Pressure Dependence of the Jahn-Teller Phonon in $La_{0.75}Ca_{0.25}MnO_3$, Phys. Rev. Lett. 86 (2001) 1251-1254.
52. A. E. Pantoja, H. J. Trodahl, R. G. Buckely, Y. Tomioka, Y. Tokura, Raman spectroscopy of orthorhombic $La_{1-x}Ca_xMnO_3$, x=0.1-0.3, J. Phys.: Cond. Matter 13 (2001) 3741-3752.
53. G. De Marzi, H. J. Trodahl, J. Bok, A. Cantarero, F. Sapiña, The effect of Cu substitution on the A_{1g} mode of $La_{0.7}Sr_{0.3}MnO_3$ manganites, Solid State Commun. 127 (2003) 259.

54. J. E. Medvedeva, V. I. Anisimov, O. N. Mryasov, A. J. Freeman, The role of coulomb in magnetic and transport properties of doped manganites: $La_{0.5}Sr_{0.5}MnO_3$ and $LaSr_2Mn_2O_7$, J. Phys. Condens. Matter 14 (2002) 4533-4542.
55. J. Ravichandran,W. Siemons, M. L. Scullin, S. Mukerjee, M. Huijben, J. E. Moore, A. Majumdar, R. Ramesh, Tunning the electronic effective mass in double –doped $SrTiO_3$, Physical Review B 83 (2011) 035101.
56. W. Wunderlicha, H. Ohta, K.Koumoto, Enhanced effective mass in doped $SrTiO_3$ and related perovskites, Physica B: Conden. Matter 404 (2009) 2202-2212.
57. C. Ma, Z. Yang, S. Picozzi,Ab-initio Electronic and Magnetic Structure in $La_{0.66}Sr_{0.33}MnO_3$: Strain and Correlation EffectsJ. Phys.: Condens. Matter 18 (2006) 7717–7728.
58. J. Li, Lizhong Sun, Prathamesh M Shenai, Junling Wang, Hang Zheng, Yang Zhao, A first - principle study of oxygen vacancy induced changes in structural, electronic and magnetic properties of $La_{2/3}Sr_{1/3}MnO_3$, J. of Alloys and Comp. 649 (2015) 973-980.
59. J. Li, The electronic, structural and magnetic properties of $La_{1-1/3}Sr_{1/3}MnO_3$ film with oxygen vacancy: a first principles investigation, Scientific Reports 6 (2016) 1-14.
60. P. Y. Vanina, A. A. Naberezhnov, V. I. Nizhankovskii, R. F. Mamin, Temperature evolution of the magnetic properties of lanthanum-strontium manganites, St. Petersburg Polytechnical University Journal: Physics and Mathematics 2 (2016) 175–180.
61. J. J. Wang, Z. Y. Guan, J. Huang, Q. X. Li, J. L. Yang, Enhanced photocatalytic mechanism for the hybrid g-C_3N_4 / MoS_2, nanocomposite, J. Mater. Chem. A 2 (2014) 7960-7966.
62. K. Cui, Y. Cheng, J. Dai, J. Liu, Synthesis characterization and microwave absorption properties of $La_{0.6}Sr_{0.4}MnO_3$/polyaniline composite, Mater. Chem. and Phys. 138 (2013) 810-816.

FIGURE CAPTIONS:

Figure 1: XRD pattern of polycrystalline $La_{0.67}Sr_{0.33}Mn_{1-x}Fe_xO_3$where (a) 0.15 (b) 0.25 and (c) 0.35.

Figure 2: SEM images of $La_{0.67}Sr_{0.33}Mn_{1-x}Fe_xO_3$(x=0.15, 0.25 and 0.35) sample prepared by solid state route.

Figure 3: EDAX spectra of $LaSrMnFeO_3$manganite system where (a) 0.15 (b) 0.25 & (c) 0.35.

Figure 4: Raman Spectra of $La_{0.67}Sr_{0.33}Mn_{1-x}Fe_xO_3$(x=0, 0.15, 0.25 and 0.35) system.

Figure 5: Electronic Density of states and Band structure of $LaSrMnFeO_3$compound where (a) 0.15 (b) 0.25 & (c) 0.35.

Figure 6: Absorption Spectra of $La_{0.67}Sr_{0.33}Mn_{1-x}Fe_xO_3$ where (a) Experimental & (b) DFT spectra of manganite system

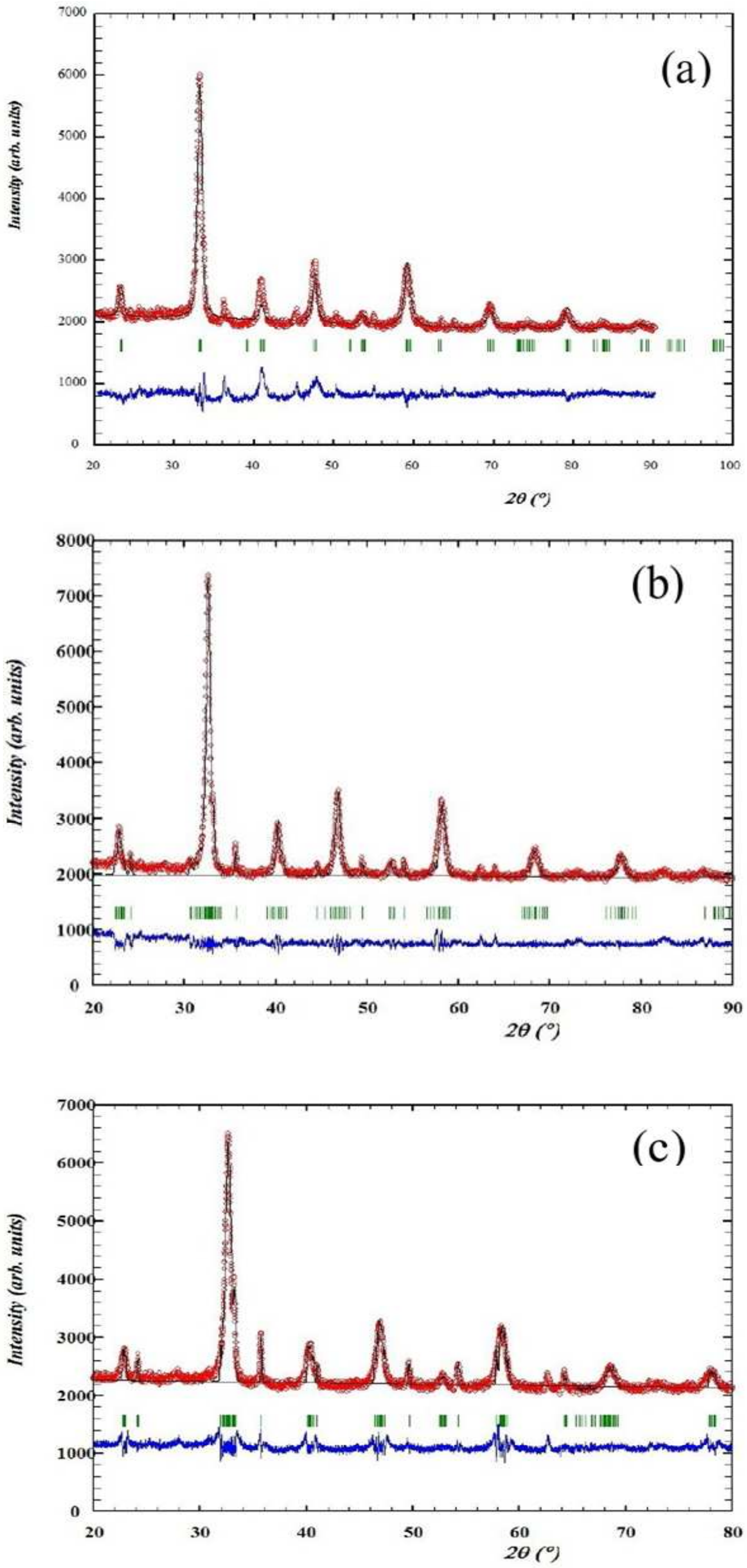
(a)
Intensity (arb. units)
7000
6000
5000
4000
3000
2000
1000
0
20
30
40
50
60
70
80
90
100
2θ (°)
(b)
Intensity (arb. units)
8000
7000
6000
5000
4000
3000
2000
1000
0
20
30
40
50
60
70
80
90
2θ (°)
(c)
Intensity (arb. units)
7000
6000
5000
4000
3000
2000
1000
0
20
30
40
50
60
70
80
2θ (°)

Fig. 1

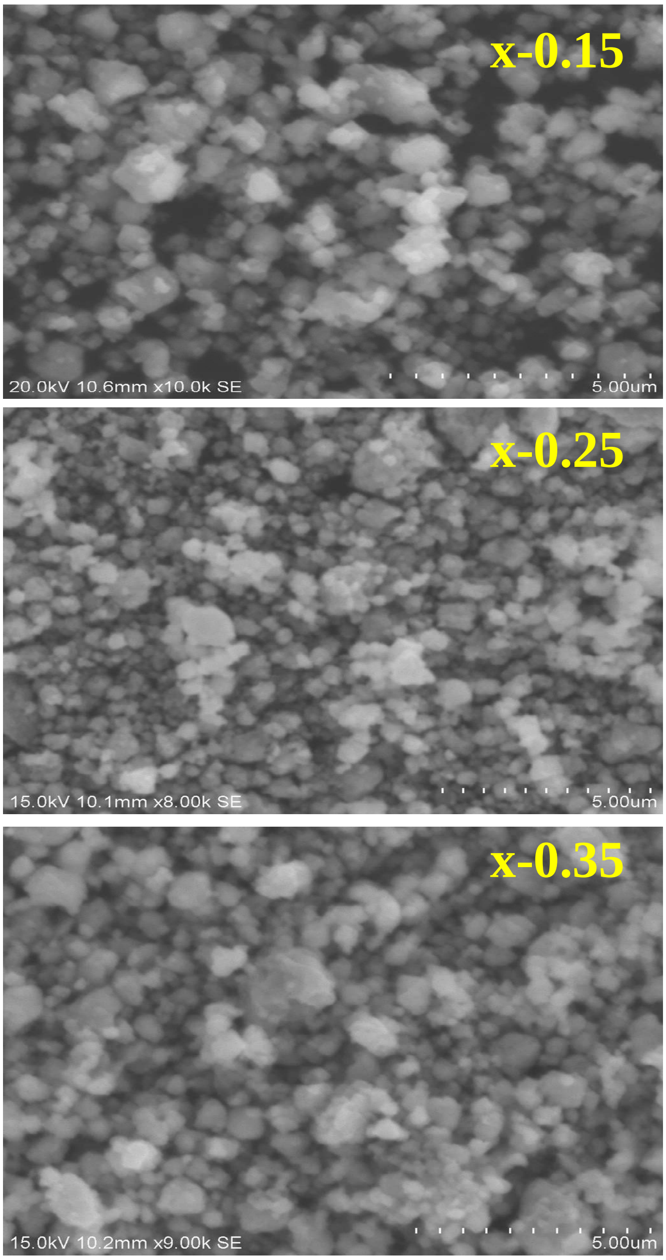
x-0.15
20.0kV 10.6mm x10.0k SE
5.00um
x-0.25
15.0kV 10.1mm x8.00k SE
5.00um
x-0.35
15.0kV 10.2mm x9.00k SE
5.00um

Fig. 2

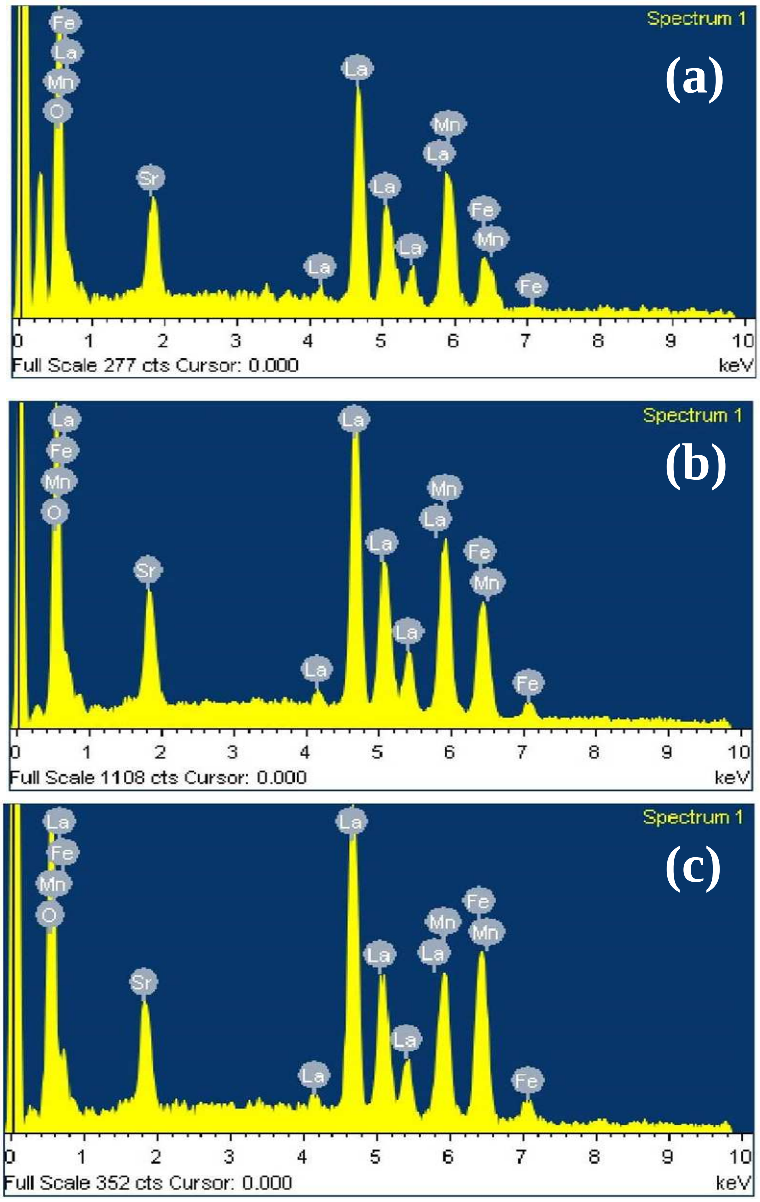
Spectrum 1
(a)
Fe
La
Mn
O
Sr
La
La
La
La
Mn
La
Fe
Mn
Fe
0 1 2 3 4 5 6 7 8 9 10
Full Scale 277 cts Cursor: 0.000
keV
Spectrum 1
(b)
La
Fe
Mn
O
Sr
La
La
La
Mn
La
Fe
Mn
Fe
0 1 2 3 4 5 6 7 8 9 10
Full Scale 1108 cts Cursor: 0.000
keV
Spectrum 1
(c)
La
Fe
Mn
O
Sr
La
La
La
La
Mn
La
Fe
Mn
Fe
0 1 2 3 4 5 6 7 8 9 10
Full Scale 352 cts Cursor: 0.000
keV

Fig. 3

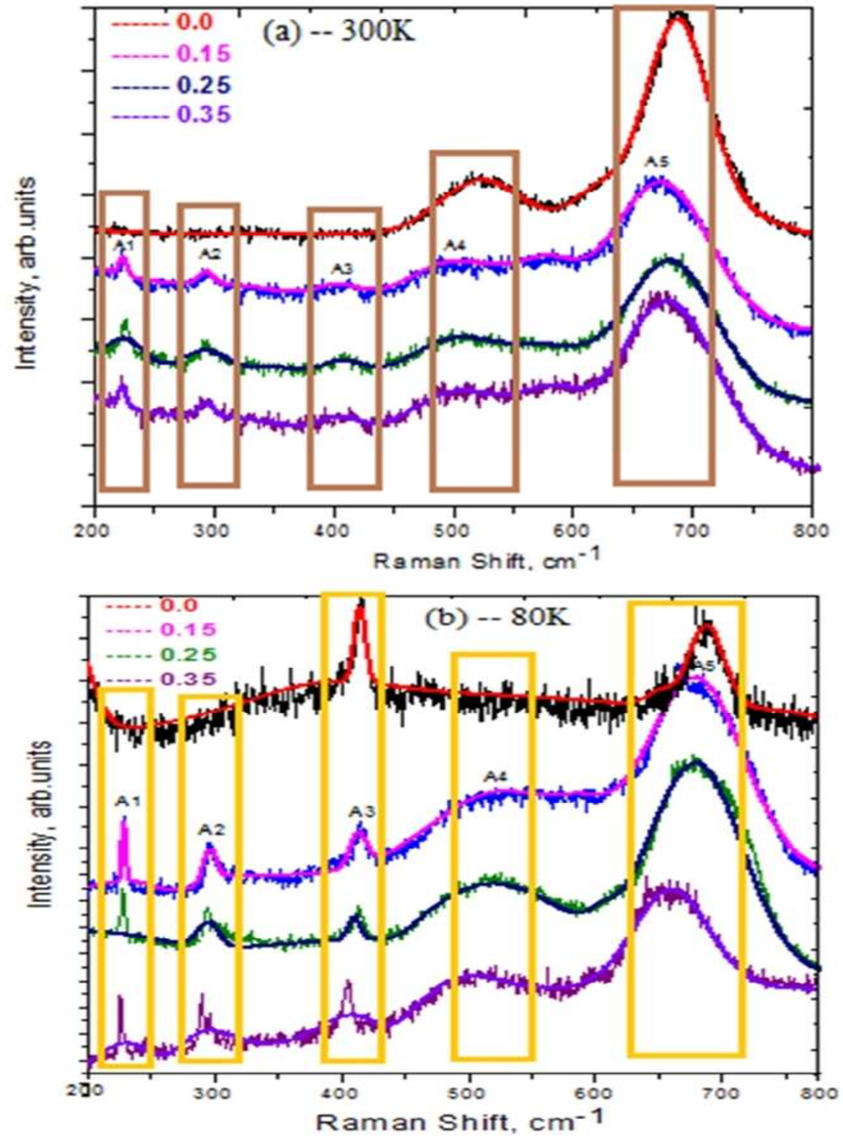
0.0
0.15
0.25
0.35
(a) -- 300K
A1
A2
A3
A4
A5
Intensity, arb.units
200
300
400
500
600
700
800
Raman Shift, cm-1
0.0
0.15
0.25
0.35
(b) -- 80K
A1
A2
A3
A4
A5
Intensity, arb.units
200
300
400
500
600
700
800
Raman Shift, cm-1

Fig. 4

(b)

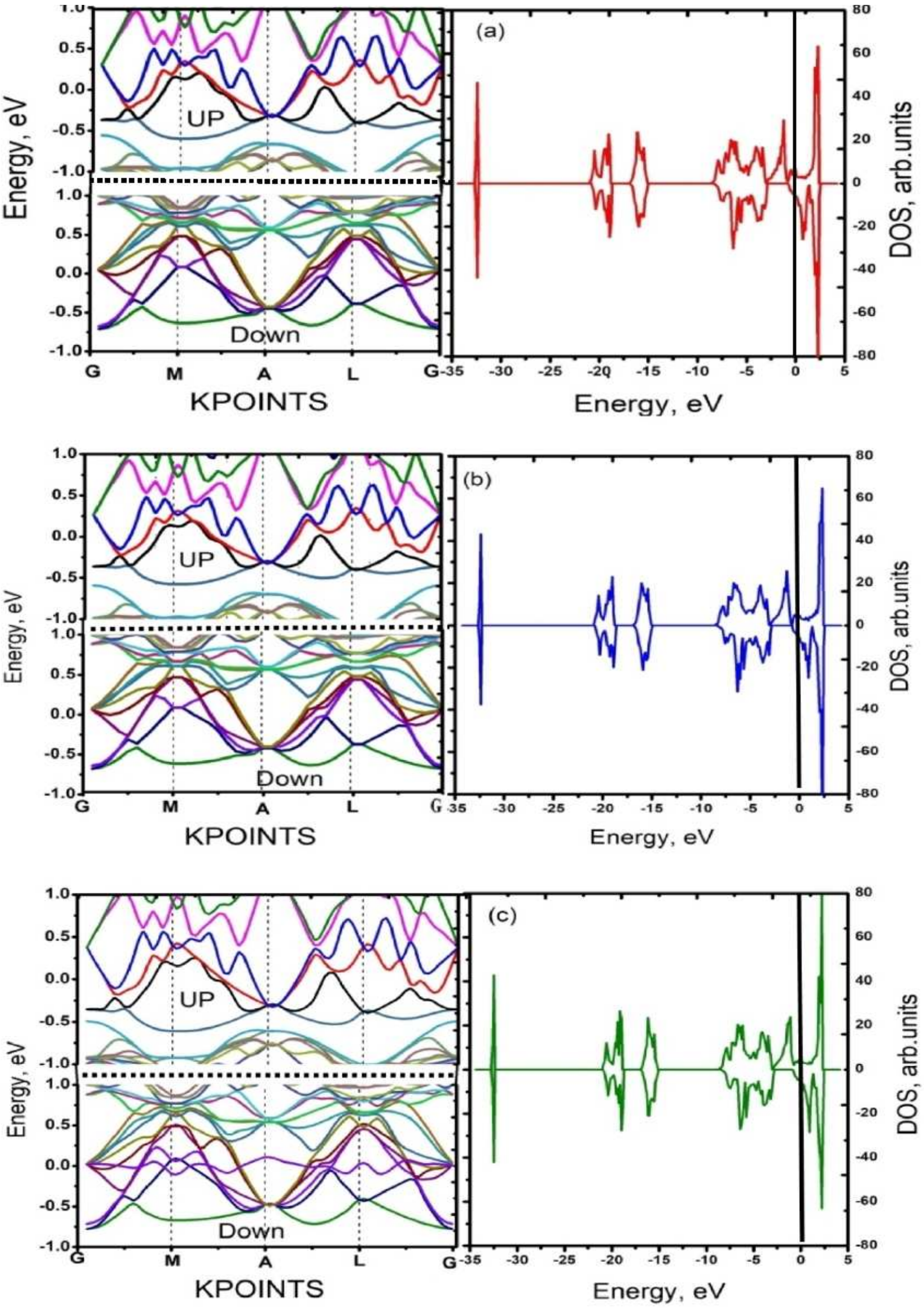
(a)
(b)
(c)
UP
Down
Energy, eV
KPOINTS
G
M
A
L
G
1.0
0.5
0.0
-0.5
-1.0
Energy, eV
DOS, arb.units
-35
-30
-25
-20
-15
-10
-5
0
5
80
60
40
20
0
-20
-40
-60
-80

Fig. 5

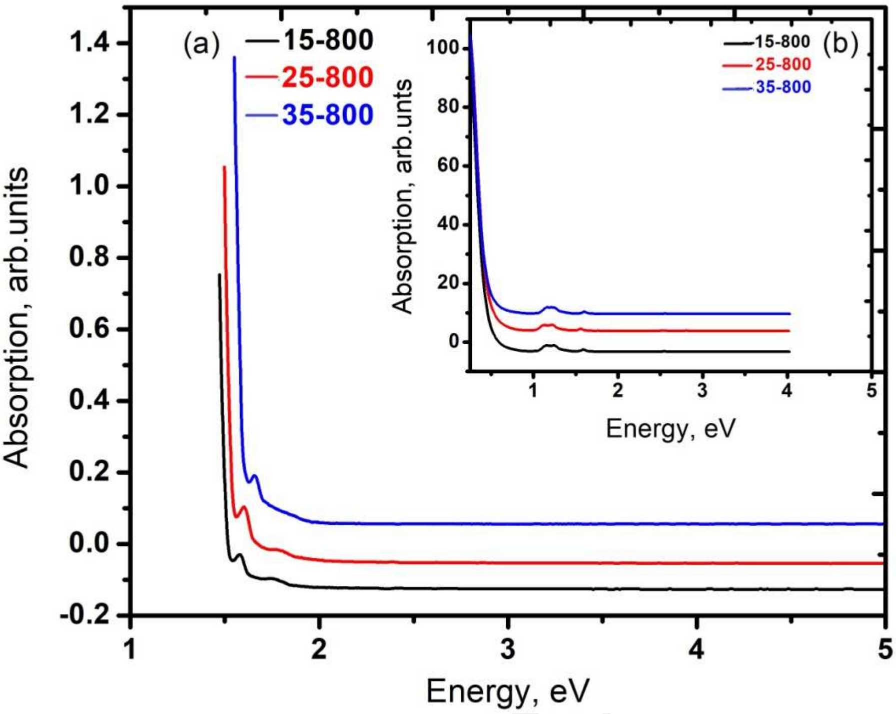
(a)
15-800
25-800
35-800
Absorption, arb.units
Energy, eV
1.4
1.2
1.0
0.8
0.6
0.4
0.2
0.0
-0.2
1
2
3
4
5
(b)
100
80
60
40
20
0
Absorption, arb.units
Energy, eV

Fig. 6

Table 1

Lattice Parameter, Crystallite Size and Unit cell volume of $La_{0.67}Sr_{0.33}Mn_{1-x}Fe_xO_3$ manganite

Sample	Structure type	Space group	Profile Fitting Function	*Lattice parameter*	a (Å)	b (Å)	c (Å)	V (Å³)	*La/Sr (6a)* x	y	z	*Mn/Fe (6b)* x	y	z	*O (18e)* x	y	z	*Discrepancy Factors (%)* R_{wp}	R_p	R_e	Goodness of Fitting (χ^2)	Particle
x=0.3 (DFT)	Rhombohedral	R-3c	Pseudo-voigt	R-3c	5.3352	5.3352	13.112		0.000	0.000	0.250	0.000	0.000	0.000	0.465	0.000	0.250	---	---	---	---	
x=0.2 (DFT)	Rhombohedral	R-3c	Pseudo-voigt		5.3900	5.3900	13.040	328.10	0.000	0.000	0.250	0.000	0.000	0.000	0.453	0.000	0.250	---	---	---	---	
x=0.1 (DFT)	Rhombohedral	R-3c	Pseudo-voigt		5.39851	5.39851	13.050	327.74	0.000	0.000	0.250	0.000	0.000	0.000	0.452	0.000	0.000	---	---	---	---	
x=0.3 (Exp)	Rhombohedral	R-3c	Pseudo-voigt		5.5129	5.5129	13.590	357.088	0.000	0.000	0.250	0.000	0.000	0.000	0.535	0.000	0.250	27.3	67.1	16.1	1.69	
x=0.2 (Exp)	Rhombohedral	R-3c	Pseudo-voigt		5.4201	5.4201	13.186	335.99	0.000	0.000	0.250	0.000	0.000	0.000	0.547	0.000	0.250	21.6	37.0	15.0	1.44	
x=0.1 (Exp)	Rhombohedral	R-3c	Pseudo-voigt		5.4194	5.4194	13.170	334.99	0.000	0.000	0.250	0.000	0.000	0.000	0.458	0.000	0.250	23.2	38.7	17.6	1.31	

Table 2

EDAX analysis of prepared samples

Samples	La	Sr	Mn	Fe	O
x=0.15	10.98	3.97	11.03	3.73	70.29
x=0.25	13.85	4.03	12.28	8.46	61.38
x=0.35	13.27	3.61	9.66	12.74	60.73

Table 3

Comparison of Raman mode position (cm^{-1}) from the Experimental and calculated by DFT study

Raman Modes	$La_{0.67}Sr_{0.3}Mn_{1-x}Fe_xO_3$ (EXP) at 300K				DFT		
	x=0	x=0.15	x=0.25	x=0.35	x=0.15	x=0.25	x=0.35
A_{1g}	252	224	225	221	226	229	221
E_g	294	292	292	286	298	295	299
E_g	513	409	409	405	409	417	410
E_g	678	670	675	675	686	671	675

Table 1: Lattice Parameters, Crystallite Size and Unit cell volume of $La_{0.67}Sr_{0.33}Mn_{1-x}Fe_xO_3$ manganite

Sample	x = 0.15 (Exp)	x = 0.25 (Exp)	x = 0.35 (Exp)	x = 0.15 (DFT)	x = 0.25 (DFT)	x = 0.35 (DFT)
Structure	Rhombohedral	Rhombohedral	Rhombohedral	Rhombohedral	Rhombohedral	Rhombohedral
Space Group	R-3c	R-3c	R-3c	R-3c	R-3c	R-3c
Profile Fitting Function	Pseudo-voigt	Pseudo-voigt	Pseudo-voigt	Pseudo-voigt	Pseudo-voigt	Pseudo-voigt
Lattice Parameters						
a (Å)	5.4194	5.4201	5.5129	5.3851	5.3900	5.3552
b (Å)	5.4194	5.4201	5.5129	5.3851	5.3900	5.3552
c (Å)	13.1700	13.1860	13.5900	13.0500	13.0400	13.1120
V ($Å^3$)	334.9900	335.9900	357.8800	327.7400	328.1000	-
La/Sr (6a)						
x	0.000	0.000	0.000	0.000	0.000	0.000
y	0.000	0.000	0.000	0.000	0.000	0.000
z	0.250	0.250	0.250	0.250	0.250	0.250
Mn/Fe (6b)						
x	0.000	0.000	0.000	0.000	0.000	0.000
y	0.000	0.000	0.000	0.000	0.000	0.000
z	0.000	0.000	0.000	0.000	0.000	0.000
O (18e)						
x	0.458	0.547	0.535	0.452	0.453	0.465
y	0.000	0.000	0.000	0.000	0.000	0.000
z	0.250	0.250	0.250	0.000	0.250	0.250
Discrepancy Factors (%)						
R_{wp}	23.2	21.6	27.3	-	-	-
R_p	38.7	37.0	67.1	-	-	-
R_e	17.6	15.0	16.1	-	-	-
Goodness of Fitting (χ^2)	1.31	1.44	1.69	-	-	-
Particle Size (nm)	21	24	27	-	-	-

Table 2: EDAX analysis of prepared samples

Samples	La	Sr	Mn	Fe	O
x=0.15	10.98	3.97	11.03	3.73	70.29
x=0.25	13.85	4.03	12.28	8.46	61.38
x=0.35	13.27	3.61	9.66	12.74	60.73

Table 3: Comparison of Raman mode position (cm^{-1}) from the Experimental and calculated by DFT study

Raman Modes	**$La_{0.67}Sr_{0.3}Mn_{1-x}Fe_xO_3$ (Exp) at 300K**				**DFT**		
	x=0	**x=0.15**	**x=0.25**	**x=0.35**	**x=0.15**	**x=0.25**	**x=0.35**
A_{1g}	252	224	225	221	226	229	221
E_g	294	292	292	286	298	295	299
E_g	513	409	409	405	409	417	410
E_g	678	670	675	675	686	671	675

Journal of ELECTRONIC MATERIALS, Vol. 47, No. 3, 2018
https://doi.org/10.1007/s11664-017-5994-7

Structural, Morphological, Differential Scanning Calorimetric and Thermogravimetric Studies of Ball Milled Fe Doped Nanoscale $La_{0.67}Sr_{0.33}MnO_3$ Manganite

NIDHI ASTIK,[1] PRAFULLA K. JHA,[1,3] and ARUN PRATAP[2]

1.—Department of Physics, Faculty of Science, The M. S. University of Baroda, Vadodara 390002, India. 2.—Department of Applied Physics, Faculty of Technology and Engineering, The M. S. University of Baroda, Vadodara 390001, India. 3.—e-mail: prafullaj@yahoo.com

The ball milling route has been used to produce the $La_{0.67}Sr_{0.33}Mn_{0.85}Fe_{0.15}O_3$ (LSMFO) nanocrystalline sample from oxide precursors. The sample was characterized using x-ray diffraction (XRD), a scanning electron microscope (SEM), energy dispersive x-ray spectroscopy (EDAX), differential scanning calorimetry (DSC) and thermogravimetric (TGA) measurements. The x-ray diffraction confirms the phase purity of sample and shows that the sample crystallizes in the rhombohedral perovskite structure with a R-3c space group. The scanning electron micrograph shows the presence of well-faceted crystallites of LSMFO. The EDAX spectrum demonstrates the molar ratio of different elements of nanocrystalline LSMFO. Furthermore, the crystallite size using the Debye–Scherrer formula and William-Hall analysis has been found as 24 nm and 29 nm, respectively. Our results support the idea that a good quality nanocrystalline LSMFO sample can be obtained using the ball milling route. We also discuss the DSC and TGA curves and analyse the results in terms of phase transition, calcination temperature and activation barrier energies.

Key words: Manganites, ball-milling, calcinations, XRD, SEM-EDAX, DSC, TGA

INTRODUCTION

There has been continuing interest in the study of doped rare-earth manganite perovskites with general formula $Ln_{1-x}A_xMnO_3$, (where Ln = La, Nd, Sm… rare earth ions and A = Ba, Sr, Pb and Ca; divalent alkaline earth ions) due to their peculiar physical properties arising from the strong coupling between spin, charge, orbit and lattice degrees of freedom and observed colossal magnetoresistance (MR) effect in them.[1–9] These doped manganites exist in a verity of phases of perovskite structure and have their potential applications in transducer and sensor, catalysis, permanent magnets, high temperature superconducting, novel electronic materials and solid oxide fuel cells.[10–17] It is a widely recognized fact that the pairs of Mn^{3+} and Mn^{4+} ions play a major role in double exchange (DE) interaction for the ferromagnetic and metallic properties in these manganese oxides. The DE effect arises due to the exchange of electrons from neighbouring Mn^{3+} to Mn^{4+} ions through oxygen when their core spins are parallel and hopping is not favoured for anti-parallel spins.[18] Furthermore, an additional mechanism, Jahn–Teller distortion (JT), has also been found responsible for the transport properties in these compounds. The JT effect causes further degeneracy of the e_g orbital of the Mn^{3+} in MnO_6 octahedral and results in electrical transport via hopping.[19–21] There are several methods, such as the solid state reaction, sol–gel and ball milling for the preparation of homogeneous samples of these materials required in various industrial applications.[22–24] It is found that the substitution of

---

(Received July 8, 2017; accepted November 22, 2017;

lanthanum or manganese by another ion in manganites directly modifies their characteristic properties due to new interactions in the La–O and Mn–O networks.[25]

The substitution of other transition elements at the Mn site of $La_{0.67}Sr_{0.33}MnO_3$ (LSMO) significantly influences the properties of these manganites, particularly the Curie temperature (T_C) due to the changes in the average electron concentration and the shifts in the position of the e_g and t_g subbands.[26–28] In this regard, the substitution of Fe ions is of particular interest as they do not only replace Mn ions extensively but also serve to fine tune the DE mechanism by breaking of the DE chain, which further weakens in strength with Fe concentration.[29–32] Furthermore, the significance of the Fe doped LSMO manganites is that the almost similar ionic radii of Fe and Mn helps in studying the local electronic structure without any lattice distortion. The doping by Fe^{3+} also seems appropriate as Fe^{3+} is magnetic and does not give rise to the JT effect and participates in the DE mechanism.[31] The 10% Fe doping results in a marked decrease in T_C and a continuous decrease in magnetic moment with Fe.[28,31] The replacement of Mn by Fe favours an insulating character and antiferromagnetism opposing the effects of double exchange.[31] The neutron diffraction study shows the existence of antiferromagnetic and ferromagnetic short range ordered regions within the samples of 20% Fe doping.[32] In addition, the modifications in the Mn^{3+}–O–Mn^{4+} network, responsible for the double exchange, can also be brought about by doping at the Mn site itself.[33–35] The Fe doping modifies the Mn^{3+}–O–Mn^{4+} network and increases the resistivity by not participating in the DE and shows a magnetic nature for LSMO samples.[36,37]

It is an established fact that the size reduction down to nanoscale modifies the magnetic and electronic properties of a material such as superparamagnetism, large coercivities, low saturation magnetization and spin glass.[9,38,39] Therefore, it will be interesting to study the magnanites with particle size comparable to magnetic domain size and develop a better understanding of the mechanism of colossal magnetoresistance. It is found that the ferromagnetism (FM) weakens at nanoscale, and Curie temperature decreases with decreasing size.[37,40] The cell volume and anisotropy of the unit cell of orthorhombic $La_{0.67}Ca_{0.33}MnO_3$ powders of 30 nm size reduce in comparison to their bulk counterpart.[41] Prellier et al.[37] have shown that the manganites of different sizes exhibit different evolution trends for lattice parameters at room temperature. The increase in the number of grain boundaries and defects at the grain surface significantly modifies the transparent behavior of nanoscale manganites.[38,39] Furthermore, in the case of nanocrytalline samples, the surface contribution to MR increases with the reduction of grain size in the temperature range between 77 K to 300 K at 1000 Oe magnetic field.[42]

In the present paper, we report structural, morphological and thermal properties of the polycrystalline $La_{0.67}Sr_{0.33}Mn_{0.85}Fe_{0.15}O_3$ (LSMFO) sample prepared by the mechanical ball milling synthesis method. The mechanical ball milling technique is one of the important techniques in powder metallurgy because of high flexibility, simple control of process parameters and ability to produce a wide range of materials. The ball milling method has been quite successful in producing single phase $Ln_xA_{1-x}MnO_3$ (Ln = La, Nd, Sm… and A = Ba, Sr, Pb and Ca) nanoparticles.[43,44] We have chosen the $x = 0.15$ concentration of Fe ions at the Mn sites in the present study, because it has a largest MR near room temperature and has the most practical applications.[45,46] For structural, morphological, elemental and thermal characterization, we have used the x-ray diffraction, scanning electron microscope, energy dispersive x-ray spectroscopy and differential scanning calorimetry and thermogravimetric analysis, respectively.

EXPERIMENTAL PROCEDURES

In this work, a pure phase of polycrystalline LSMFO manganite has been prepared by the standard solid state reaction method using the mixture of precursors MnO_2, La_2O_3, SrO and Fe_2O_3 up to 99.9% purity in the appropriate stoichiometry molar amounts. These materials were milled in PULVERISETTE—5 planetary ball mills.[47] The rotation speed was chosen to be 250 rpm, while the ball to powder ratio was 10:1. The mixture of powders was milled for 8 h and then the obtained powder was calcined at 1000°C. The details are shown in Table I.

Phase purity, homogeneity, and crystal properties were determined by powder x-ray diffraction at room temperature using a PANalytical X'Pert Pro diffractometer with CuKα radiation ($\lambda = 1.5406$ Å). Diffraction data were collected over the 2θ range of 20° to 100°. The composition and surface morphology of resulting products were investigated using a JEOL JMS-5610LV scanning electron microscope and molar ratio of elements in samples was evaluated by Oxford INCA Energy Dispersive analysis of

Table I. Parameters of milling balls and raw materials

Raw materials	Mol ratio/mol	Mass/g	Total mass/g
La_2O_3	0.022	7.16	15.67
SrO	0.021	2.17	
MnO_2	0.056	4.86	
Fe_2O_3	0.0093	1.4	

x-rays (EDAX). Thermal analysis was carried out using a DSC-50, Shimadzu differential scanning calorimetry (DSC) by heating the sample at 5°C/min in a thermal analyzer in the presence of air. The thermogravimetric analysis was carried out with a TGA-50, Shimadzu at the heating rate of 5°C/min.

RESULTS AND DISCUSSION

The powder x-ray diffraction (XRD) method is used to verify the crystal structure and phase purity of the prepared sample. The room temperature XRD pattern of the prepared polycrystalline LSMFO sample is presented in Fig. 1. The obtained XRD data have been analyzed by the Rietveld method using the FullPROF program. This figure also includes the XRD pattern after Rietveld refinement. In this method, the observed profiles are matched with the profiles constructed similarly using a pseudo-voight function. The calculated profiles have been compared with the observed ones. The obtained refined structural parameters together with the other available data are presented in Table II.[48–50] There is a good correspondence between the presented and observed data. The asterisks (*) in Fig. 1 indicate the presence of Mn_3O_4 phase in prepared samples. The vertical lines are the calculated Bragg's positions of the reflections for rhombohedral compounds. The bottom lines, showing the difference between the experimental and calculated XRD patterns, show a good agreement between the observed and calculated intensities. All the reflection lines for the parent sample successfully correspond to the rhombohedral structure belonging to the space group R-3c.[50,51] We do not observe any unfitted peaks in different spectra indicating a very small (< 1%) contribution of second phase Mn_3O_4 present in samples as seen by Khilfi et al.[52,53] We have observed the diffracted peaks of nanosamples at planes (012), (104), (202), (024) and (116) confirming the rhombohedral structure. These show ball milling to be a successful method to directly produce the stoichiometry and homogenous polycrystalline LSMFO manganites. Now, according to the Debye–Scherrer equation, the broadening due to small crystallite size can be expressed as[54]:

$$D = 0.9\lambda/\beta\cos\theta, \tag{1}$$

where D, θ and λ are the average crystallite size, Bragg's angle and wavelength of incident x-ray beam in nm, respectively. The 0.9 is shape factor and β is the instrumental corrected line broadening at half of the maximum intensity (FWHM). The average crystallite size of the LSMFO nanoparticles using the Debye–Scherrer formula is 24 nm. In the present study, we have also employed W–H analysis for estimating crystallite size and lattice strain. The Williamson–Hall (W–H) analysis is a simplified integral breadth method where both size - induced and strain- broadening are deconvoluted by considering the peak width as a function of 2θ.[54] The strain associated with the annealed LSMFO sample at 1000°C due to lattice deformation has been estimated using a modified form of W–H, namely, the uniform deformation model (UDM). The strain induced in powders due to crystal imperfection and distortion has been calculated as

$$\varepsilon = \beta_{hkl}/4\sin\theta. \tag{2}$$

A plot between 4sinθ and β_{hkl}cosθ for the polycrystalline LSMFO is shown in Fig. 2. Using UDM, the estimated crystallite size and strain from this plot comes out to be 29 nm and $1.01 \times 10^{-3,}$ respectively. The variation between average crystallite size obtained from Scherrer's formula and W–H analysis can be attributed to the difference in averaging the particle size distribution,[55] selection of crystallographic direction[56] and the account of strain through the broadening of diffraction peaks. The W–H procedure presents a correction to the problem.

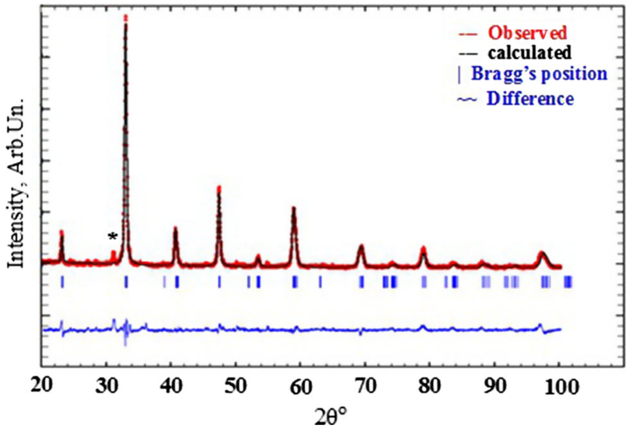

Fig. 1. XRD pattern of polycrystalline $La_{0.67}Sr_{0.33}Mn_{0.85}Fe_{0.15}O_3$ prepared by the solid state reaction.

The compositional detail of the prepared nanocrystalline LSMFO sample using energy dispersive analysis of x-rays (EDAX) is presented in Fig. 3. In this technique an electron beam of 10–20 keV strikes the surface of a sample, which causes x-rays to be emitted from the point of incidence. A photoelectron is generated during the x-ray and detector interaction. The energy of the characteristic x-ray emitted from the different elements is different, and; hence, a signature of a particular element is observed in the spectra. It can be observed from the EDAX spectra of nano LSMFO that the sample is composed of La, Sr, Mn, Fe and O atoms. The molar ratio for the elements La, Sr, Mn, Fe and O from the EDAX spectra is shown in Fig. 3, while the atomic percent is presented in Table III. The molar ratio of elements La, Sr, Mn, Fe and O is, respectively, 48.82, 8.81, 19.11, 5.96 and 17.31, which is consistent with earlier study.[57] The close agreement between the atomic ratio of La, Sr, Mn,

Table II. Details of the Rietveld refinement XRD parameters of prepared nanocrystalline powder

Parameters	$La_{0.67}Sr_{0.33}Mn_{0.85}Fe_{0.15}O_3$ (x = 0.15)		
2θ range (°)	20–100		
Step size (°)	0.0170		
Wavelength (Å)	1.5406		
Space group	R-3c		
$a = b$ (Å)	5.5038, 5.508[a], 5.524[b], 5.4927[c]		
c (Å)	13.3901, 13.357[a], 13.40[b], 13.346[c]		
Volume (Å^3)	351.28, 350.9[a], 354.3[b], 348.7[c]		
α (°)	90		
β (°)	90		
γ (°)	120		
R_f 16.2			
R_{Bragg}	12.6		
R_{wp}	17.6		
R_{exp}	12.7		
R_p	32.8		
χ^2	1.91		
GOF	1.38		
Atoms	x	y	z
La/Sr	0.0000	0.0000	0.25
Mn/Fe	0.0000	0.0000	0.25
O	0.544	0.0000	0.25

[a]Ref.48.[b]Ref.49.[c]Ref.54.

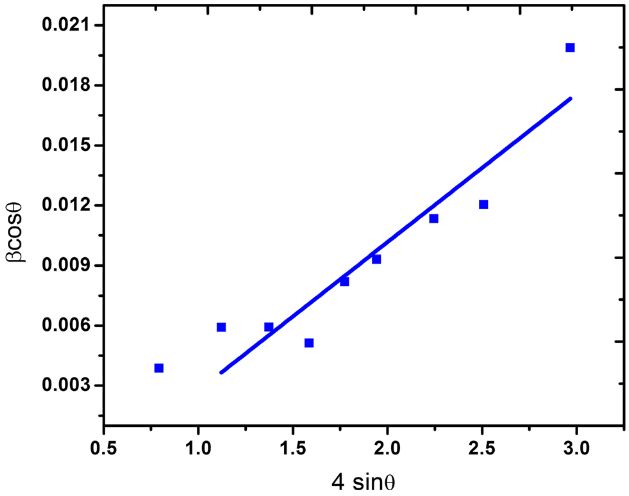

Fig. 2. Williamson–Hall plots of LSMFO manganite samples.

Fe and O atoms obtained in the present spectra and previous spectra suggests correct stoichiometric for the prepared nanoscale LSMFO perovskite. The prepared sample is pure due to the absence of any impurity peak in the sample.[58]

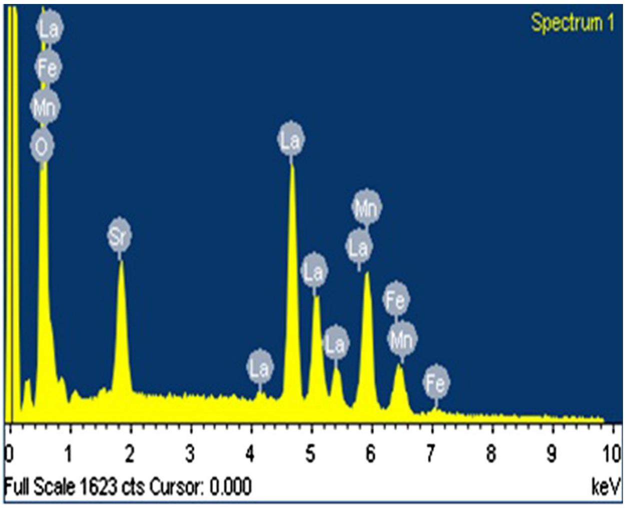

Fig. 3. EDAX spectra of LSMFO nanoscale particles.

Table III. Atomic percent of the EDAX pattern recorded of studied samples

Element	Atomic%
La	17.67
Sr	5.05
Mn	5.36
Fe	17.49
O	54.42
Total	100

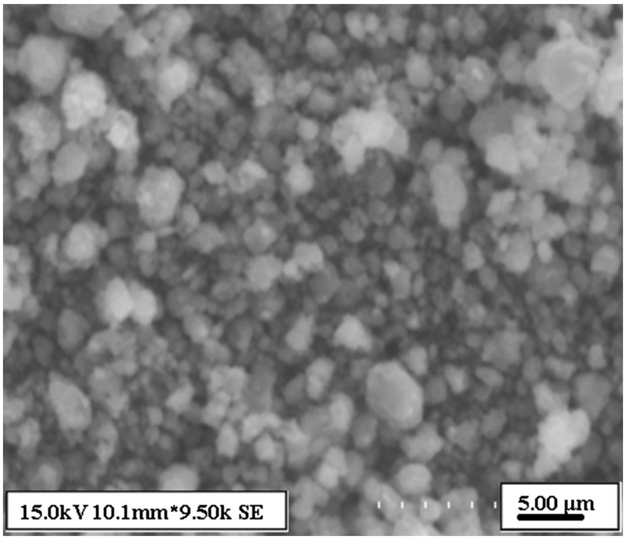

Fig. 4. SEM images of $La_{0.67}Sr_{0.33}Mn_{0.85}Fe_{0.15}O_3$ sample prepared by the solid state route.

The microscopical morphology of particles of the nanocrystalline LSMFO sample has been examined by SEM and presented in Fig. 4. The microscopic image clearly shows that most of the grains are spherical in shape with nonuniform distribution. A careful analysis of the micrograph reveals well defined grains with clear boundaries. The SEM micrograph shows that the tiny particles are agglomerated with the distance scale of 5 μm. Figure 4 also depicts that the LSMFO sample without any intermediate grinding process causes irregular grain formation, which can be attributed to homogeneity of agglomerated particles.[59] Furthermore, it is seen that the surface of particles is composed of smaller particles with irregular morphology indicating grain growth due to high temperature. The smaller grains and resulting increased ratio of the grain boundaries are expected to influence the electromagnetic transport.[60] The SEM images show the particle size of 200 nm, which may be attributed to the collection of several grains.

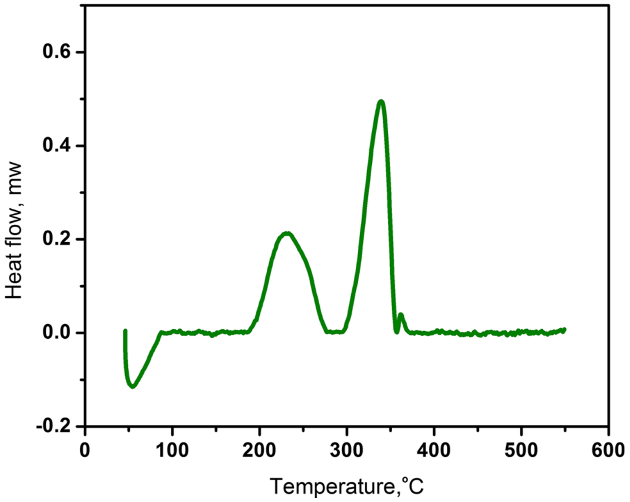

Fig. 5. DSC curves of synthesized LSMFO particles.

Now, we turn our attention to the thermal analysis of nanocrystalline LSMFO using DSC and TGA. DSC measures the amount of heat energy absorbed or released by a given sample as it is under a constant or variant heat treatment.[61] In the case of a DSC measurement, the difference in heat flow to the given sample and reference material, which is an inert material, is recorded as a function of temperature increased at constant rate. The heat flow difference between sample and reference material can be either positive (endothermic) or negative (exothermic). The endothermic peak temperature in the DSC plot can be related to the peak in the temperature variation of the magnetization curve and, hence, a magnetic transition of the first order.[62] DSC and TGA measurements for Fe doped nanoscale LSMO are shown in Figs. 5 and 6, respectively. Exothermic two steps decomposition takes place from between 200°C to 350°C. With the increase in temperature, the TGA curve shows mainly three weight loss regions. Based on the analysis of weight loss in each region, the complete thermal decomposition process can be distinguished as discussed below. The TGA curve indicates that the weight loss takes place in three steps. The total weight loss is about 30% up to 1200°C. The first weight loss is 8% up to 250°C, which can be attributed to the water evaporation and arising from moisture. The second weight loss is 17% in the temperature range 250°C to 700°C, and the final third weight loss of 5% takes place from 700°C to 1200°C. The formation of product takes place at

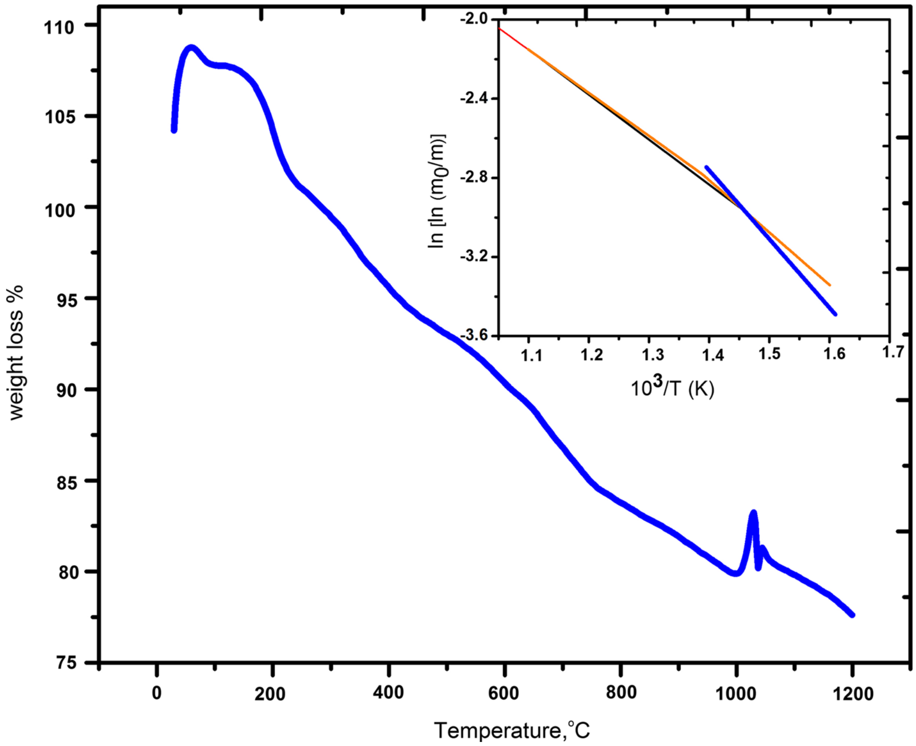

Fig. 6. TGA curves of $LaSrMnFeO_3$ particles.

1000°C, which decomposes at higher temperature. To further understand the process of heat energy absorbed or released, we have calculated the activation barrier from the TGA pattern using the following equation.[63]

$$\ln\left[\ln\left(m_0/m\right)\right] = -E/R\,(1/T) + \text{const}, \qquad (3)$$

where E is the activation barrier, m_o is the initial mass and R is the universal gas constant. The plot presented in the inset of Fig. 6 clearly shows three step processes in transition. The activation barrier turns out to be 17.69 J, 19.07 J, and 25.8 J, respectively for the temperature ranges; up to 250°C, 250°C–700°C, and 700°C–1200°C.

CONCLUSIONS

In summary, we have prepared the nanoscale iron doped $La_{0.67}Sr_{0.33}MnO_3$ polycrystalline samples by the ball milling process and investigated its structural, morphological and thermal properties. Our studies show that the high energy ball milling of La_2O_3, SrO, MnO_2, and Fe_2O_3 powders leads to the synthesis of nanosized $La_{0.67}Sr_{0.33}Mn_{0.85}Fe_{0.15}O_3$ (LSMFO) in rhombohedral phase. The crystallite size for the nano LSMFO is obtained as 24 nm and 29 nm using the Scherrer formula and W–H analysis, respectively. The SEM image clearly brings out the formation of the agglomerated particles with the distance scale of 5 μm. The compositional analysis of nanocrystalline LSMFO is also done using EDAX. The thermal analysis of the sample is done using DSC and TGA, which shows that the decomposition and weight loss are a three step process.

ACKNOWLEDGEMENTS

Financially assistance from the SERB (SR/S2/CMP-0005/2013), New Delhi is highly acknowledged. One of us, Nidhi M. Astik, is thankful to the UGC for the award of the UGC-BSR Fellowship. Authors are thankful to head Geology Department for providing the SEM facility.

REFERENCES

1. E. Dagotto, *Nanoscale Phase Separation and Colossal Magnetoresistance* (New York: Springer, 2003), pp. 9–20.
2. S. Jin, T.H. Tiefel, and M. McCormark, *Science* 264, 413 (1993).
3. A. Asamitsu, Y. Moritomo, Y. Tomioka, T. Arima, and Y. Tokura, *Nature* 373, 407 (1995).
4. Y. Tokura, *Colossal Magnetoresistive Oxides* (Netherlands: Gordon and Breach Science, 2000), pp. 1–53.
5. J.B. Goodenough, *Phys. Rev.* 100, 564 (1955).
6. M. Talati and P.K. Jha, *Phys. Rev. B* 74, 134406 (2006).
7. M. Talati and P.K. Jha, *Comput. Mater. Sci.* 37, 64 (2006).
8. Y. Tokura and Y. Tomioka, *J. Magn. Magn. Mater.* 200, 1 (1999).
9. X.H. Huang, J.F. Ding, Z.L. Jiang, Y.W. Yin, Q.X. Yu, and X.G. Li, *J. Appl. Phys.* 106, 083904 (2009).
10. P.K. Davies, H. Wu, A.Y. Borisevich, I.E. Molodetsky, and L.A. Farber, *Rev. Mater. Res.* 38, 369 (2008).
11. L. Sebastian, A. Jose, D. Sheptyakov, M. Alguero, M. Angel, P. Vladimir, and C.P. Jose, *Inorg. Chem.* 50, 5545 (2011).
12. O. Ortiz-Diaz, M.J. Rodriguez, F. Fajardo, D.A. Tellez, and J. Roa-Rojas, *Physica B* 398, 248 (2007).
13. U. Joshi and J.S. Lee, *Solid State Phenom.* 19, 275 (2007).
14. T. Tsuchiya, T. Yoshitake, Y. Shimakawa, Y. Kubo, Y. Yamaguchi, T. Manabe, T. Kumagai, and S. Mizuta, *Appl. Phys. Mater. Sci. Process.* 79, 1537 (2004).
15. A.J. Darbandi, T. Enz, and H. Hahn, *Solid State Ion.* 180, 424 (2009).
16. M. Izumi, Y. Murakami, Y. Konishi, T. Manako, M. Kawasaki, and Y. Tokura, *Phys. Rev. B* 60, 1211 (1999).
17. V.S.R. Channu, R. Holze, and E.H. Walker, *New J. Glass Ceram.* 3, 29 (2013).
18. C. Zener, *Phys. Rev.* 81, 440 (1951).
19. N. Rama, V. Sankaranarayan, and R. Rao, *J. Alloys Compd.* 466, 12 (2008).
20. E. Dagotto, T. Hotta, and A. Moreo, *Phys. Rep.* 344, 1 (2001).
21. K.P. Lim, S.W. Ng, S.A. Halim, S.K. Chen, and J.K. Wong, *Am. J. Appl. Sci.* 6, 1153 (2009).
22. H. Aono, H. Hirazawa, H. Naohara, T. Maehara, H. Kikkawa, and Y. Watanabe, *Mater. Res. Bull.* 40, 1126 (2005).
23. M. Venkatesan, S. Nawka, S.C. Pillai, and J.M.D. Coey, *J. Appl. Phys.* 93, 8023 (2003).
24. D. Thapa, V.R. Palkar, M.B. Kurup, and S.K. Malik, *Mater. Lett.* 58, 2692 (2004).
25. P.K. Siwach, H.K. Singh, and O.N. Srivastava, *J. Phys. Condens. Matter* 20, 273201 (2008).
26. S.K. Hasanain, M. Nadeem, W.H. Shah, M.J. Akhtar, and M.M. Hasan, *J. Phys. Condens. Matter* 12, 9007 (2000).
27. K. Ghosh, S.B. Ogale, R. Ramesh, R.L. Greene, and T. Venkatesan, *Phys. Rev. B* 59, 533 (1999).
28. W.H. Shah and S.K. Hasanain, *J. Mater. Res.* 26, 2599 (2011).
29. J.A. Mydosh, *Spin Glasses: An Experimental Introduction* (London: Taylor and Francis, 1993), pp. 1–256.
30. L.F. Barquin and R.G. Calderon, *J. Phys. Conf. Ser.* 17, 87 (2005).
31. J. Gutiérrez, A. Peña, J.M. Barandiarán, J.L. Pizarro, T. Hernández, L. Lezama, M. Insausti, and T. Rojo, *Phys. Rev. B* 61, 9028 (2000).
32. J. Gutiérrez, F.J. Bermejo, J.M. Barandiarán, S.P. Cottrell, P. Romano, C. Mondelli, J.R. Stewart, L. Fernández Barquín, and A. Peña, *Phys. Rev. B* 73, 054433 (2006).
33. E. Banks and N. Tashima, *J. Appl. Phys.* 41, 1186 (1970).
34. G.H. Jonker, *Physica* 20, 1118 (1954).
35. A.V. Deshmukh, S.I. Patil, S.M. Bhagat, P.R. Sagdeo, R.J. Choudhary, and D.M. Phase, *J. Phys. D Appl. Phys.* 42, 185410 (2009).
36. M.M. Xavier Jr., F.A.O. Cabral, J.H. Araujo, C. Chesman, and T. Dumelow, *Phys. Rev. B* 63, 012408 (2000).
37. W. Prellier, P. Lecoeur, and B. Mercey, *J. Phys. Condens. Matter* 13, 915 (2001).
38. T. Zhang, X.P. Wang, Q.F. Fang, and X.G. Li, *Appl. Phy. Rev.* 1, 031302 (2014).
39. Y. Wang and H.J. Fan, *Small* 8, 1060 (2012).
40. M.A. López-Quintela, L.E. Hueso, J. Rivas, and F. Rivadulla, *Nanotechnology* 14, 212 (2003).
41. S. Shankar, S. Kar, G.N. Subbanna, and A.K. Raychaudhuri, *Solid State Commun.* 129, 479 (2004).
42. B.X. Huang, Y.H. Liu, R.Z. Zhang, X. Yuan, C.J. Wang, and L.M. Mei, *J. Phys. D Appl. Phys.* 36, 1923 (2003).
43. S. Kaliaguine, A. van Neste, V. Szabo, J.E. Gallot, M. Bassir, and R. Muzychuk, *Appl. Catal. A* 209, 345 (2001).
44. L. Manh, T.K. Anh, D.X. Loc, T.T. Huong, and N. Vu, *Int. J. Nanotechnol.* 8, 335 (2011).
45. A. Urishibara, Y. Morimoto, T. Arima, A. Asamitsu, G. Kido, and Y. Tokura, *Phys. Rev. B* 51, 14103 (1995).
46. M. Bibes and A. Barthelemy, *IEEE Trans. Electron. Devices* 54, 1003 (2007).
47. G. Campillo, A. Gil, O. Arnache, J.J. Beltran, J. Osorio, and G. Sierra, *J. Phys. Conf. Ser.* 466, 012022 (2013).
48. D.H. Manh, P.T. Phong, P.H. Nam, D.K. Tung, N.X. Phuc, and I.-J. Lee, *Physica B* 444, 94 (2014).

49. M. van den Bossche† and S. McIntosh, *Chem. Mater.* 22, 5856 (2010).
50. D. Varshney and M.A. Dar, *J. Alloys Compd.* 619, 122 (2015).
51. Y. Shlapa, M. Kulyk, V. Kalita, T. Polek, A. Tovstolytkin, J.M. Greneche, S. Solopan, and A. Belous, *Nanoscale Res. Lett.* 11, 1 (2016).
52. M. Khlifi, M. Bejar, O. EL Sadek, E. Dhahri, M.A. Ahmed, and E.K. Hlil, *J. Alloys Compd.* 509, 7410 (2011).
53. D. Fatnassi, J.L. Rehspringer, E.K. Hlil, D. Niznansky, M. Ellouze, and F. Elhalouani, *J. Supercond. Nov. Magn.* 287, 2401 (2015).
54. C. Suryanarayana and M.G. Norton, *X-Ray Diffraction: A Practical Approach* (New York: Springer, 1998), pp. 1–273.
55. M. Parra and F.Z. Haque, *J. Mater. Res. Technol.* 3, 363 (2014).
56. N.S. Gonclaves, J.A. Carvalho, Z.M. Lima, and J.M. Sasaki, *Mater. Lett.* 72, 36 (2012).
57. Z.F. Zi, Y.P. Sun, X.B. Xhu, Z.R. Yang, J.M. Dai, and W.H. Song, *J. Magn. Magn. Mater.* 321, 2378 (2009).
58. N.D. Thorat, K.P. Shinde, S.H. Pawar, K.C. Barick, C.A. Betty, and R.S. Ningthoujam, *Dalton Trans.* 41, 3060 (2012).
59. C.H. Wei, L.K. Pah, A.H. Shaari, C.S. Kien, A. Gan, N.S. Wei, and W.J. Kuen, *Solid State Sci. Technol.* 20, 148 (2012).
60. S. Chen, C. Yang, L. Xu, and S. Tang, *J. Mater. Sci. Technol.* 26, 721 (2010).
61. J. O'neil Michael and S. Watson Emmett, U. S. Patent 484, 3, 263 (1966).
62. I. Dhiman, A. Das, P.K. Mishra, and L. Panicker, *Phys. Rev. B* 77, 09440 (2009).
63. A. Pandey, A. Pratap, D. Bhattacharya, and R.G. Sharma, *Physica C* 341, 2449 (2000).

Synthesis and characteristic of nanocrystalline La0.7Sr0.3MnO3 manganites by solid state reaction route

Nidhi Astik, Swapnilkumar Patil, Parag Bhargava, and Prafulla K. Jha

Citation: AIP Conference Proceedings **1728**, 020467 (2016); doi: 10.1063/1.4946518
View online: http://dx.doi.org/10.1063/1.4946518
View Table of Contents: http://scitation.aip.org/content/aip/proceeding/aipcp/1728?ver=pdfcov
Published by the AIP Publishing

Synthesis and Characteristic of Nanocrystalline $La_{0.7}Sr_{0.3}MnO_3$ Manganites by Solid State Reaction Route

Nidhi Astik[1,a], Swapnilkumar Patil[2,b], Parag Bhargava[3] and Prafulla K Jha[1]

[1] *Department of physics, Faculty of Science, The M. S. University of Baroda, Vadodara*
[2] *Department of Physics, M. K. Bhavnagar University, Bhavnagar*
[3] *Department of Metallurgical Engineering & Material Science, IIT-Bombay, India*

[a] *nidhiastik2002@gmail.com* , [b] *patilswapnilkumar@yahoo.co.in*

Abstract. Nanocrystalline stoichiometric $La_{0.7}Sr_{0.3}MnO_3$ (x=0.3) manganites have been synthesized through solid-state reaction by ball milling mechanical method at two different sintering temperatures 1250°C and 1350°C. The synthesized samples were characterized using X-ray diffraction (XRD) and found to have rhombohedral crystal structure (R-3c). The calcined samples exhibited a pure single phase perovskite, had a crystallite size of about 47-51 nm. The morphology of the prepared nanocrystalline manganites were recorded by the field emission gun-scanning electron microscope (FEG-SEM) and EDAX.

INTRODUCTION

The perovskite manganites of type $R_{1-X}A_XMnO_3$ where R is La^{3+}, Pr^{3+}, Nd^{3+} and A is Ca^{2+}, Sr^{2+}; received great deal of attention in last decades due to their unusual magnetic and transport properties, especially the colossal magnetoresistance (CMR) [1-3]. The strontium doped perovskite – type manganites $La_{1-X}Sr_XMnO_3$ (LSMO) have attracted remarkable interest due to their various potential applications such as magnetic sensors, reading heads for magnetic memories and as a cathode in solid oxide fuel cells due to its excellent catalytic, thermal, electrical, phonon and magnetic properties [4-8]. The properties of these materials are governed by several factors such as method of preparation, doping percentage and size of divalent ions [9-11]. In addition, these manganites have attracted much attention in recent time due to colossal magnetoresistance effect [12] and their intriguing physics. The colossal magnetoresistance in a strongly correlated electron system arises due to strong interactions among the charge, spin, orbital and lattice degree of freedom, such as double-exchange interaction, super-exchange interaction, Jahn-Teller type electron-lattice distortion, Hund's coupling etc., leading to complex structural, magnetic and electronic phase diagrams. Furthermore, the $La_{0.7}Sr_{0.3}MnO_3$ (LSMO) amongst several other manganites is of particular interest due to its high T_c of 380 K, a large magnetic moment at room temperature and highest magnetoresistance (MR) near the room temperature [13-15]. Several preparation techniques to synthesize these materials such as mechanochemical, sol-gel, co-precipitation and solid state reaction have been developed. However, the solid state route has been recognized as a powerful method for the production of novel, high performance as well as low cost materials such as ferrites, intermetallic etc [16-18].

In this work, an effort has been made to synthesize Sr doped $LaMnO_3$ system in nano regime i.e. $La_{1-X}Sr_XMnO_3$ (x=0.3) nanoparticles by solid state reaction method. We also present the effect of sintering temperature on structure of these nanocrystalline $La_{0.7}Sr_{0.3}MnO_3$ manganites.

EXPERIMENTAL PROCEDURE

Magnetic nanoparticles of $La_{1-x}Sr_xMnO_3$ (LSMO) x = 0.3 were prepared via conventional solid state reaction method by mechanical ball milling method using ingredients La_2O_3 (99.9%), SrO_2 (99.9%) and MnO_3. Stoichiometric amounts of starting compounds are mixing for 3h and sintering at 1250 and 1350°C for several hours with intermediate grinding steps using 250 rpm. The powder was subjected to the mechanical milling process in air

International Conference on Condensed Matter and Applied Physics (ICC 2015)
AIP Conf. Proc. 1728, 020467-1–020467-4; doi: 10.1063/1.4946518
Published by AIP Publishing. 978-0-7354-1375-7/$30.00

atmosphere, by using a planetary ball milling Fritsh PULVERISETTE 5. The structural characterization was explored by X-ray diffraction (XRD) using CuKα radiation at room temperature. Surface morphology and compositions were studied by FEG-SEM analysis and Energy dispersive analysis of X-ray respectively.

RESULTS AND DISCUSSIONS

The XRD results of the prepared LSMO nanoparticles at 1250 and 1350°C are shown in Fig. 1. For LSMO samples prepared at 1250°C, the perovskite structure is seen to be superior in the sample with x=0.3. The diffraction patterns of $La_{0.7}Sr_{0.3}MnO_3$ perovskite nanostructures reveal all characteristic peaks of the perovskite phase**.** The obtained LSMO samples are in single phase without any secondary or impurity phase. The confirmed compound formation belongs to the rhombohedral crystal symmetry of space group R-3C similar to the one obtained refs. [19-20]. The Diffraction peaks at angle 2Θ ~ 32.09 represents the 110 plane of perovskite phase.

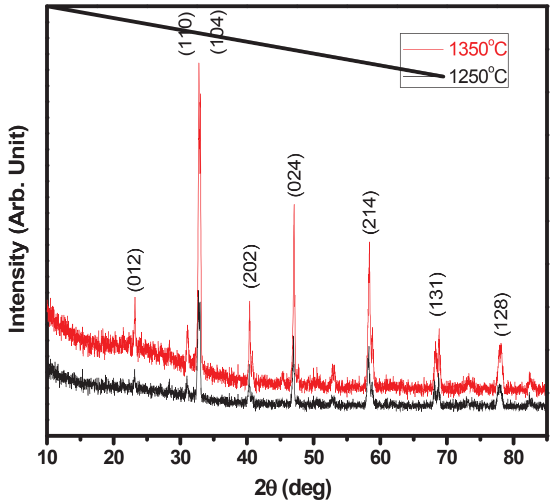

FIGURE 1. XRD pattern of $La_{0.7}Sr_{0.3}MnO_3$ sintered at different temperatures 1250 and 1350°C

We have also calculated the lattice parameters and presented them in Table 1. There is a good agreement with the earlier reported values [21-23]. However, there is an increase in unit cell volume for sample with high sintering temperature. The crystallite size of the compound was calculated from the broadening of the strong and medium reflections of (012), (110), (202), (024), (214), (131) using Debye –Scherer's formula,

$$d = \frac{K}{\beta}$$

Where K is the shape factor which is taken as 0.9, λ is the wavelength of Cu Kα radiation (λ=1.5406), and β is the full width at half maxima (FWHM) of the peak corresponding to the maximum intensity and Θ represents the diffraction angle of the most intense peak in degrees [24]. As we have used the powder samples, the XRD peak broadening due to mechanical strain, instrumental error and other sources have been ignored in the calculation of the crystallite size. The average crystallite size of the LSMO sample lies in between 47 and 51 nm for the sample calcined at 1250^0 C and 1350^0 C respectively. Further, the Table 1 shows that the crystallite size of the LSMO samples increases significantly with increasing the calcinations temperature. However, the procedure of finding average crystallite size using Scherrer's formula is an indirect way to estimate the size approximately.

TABLE 1. Lattice Parameters, Unit Cell volume and crystallite size of $La_{0.7}Sr_{0.3}MnO_3$ samples.

Sample	**Lattice Parameter** a(Å)	b(Å)	c(Å)	**Unit Cell Volume V, (pm$^{3)}$**	**Crystallite Size D (nm)**
SM0312	5.48	5.48	13.31	0.346	47
SM0313	5.49	5.49	13.33	0.348	51

A quantitative EDAX analysis is used to determine the composition x=0.3 of LSMO in Fig. 2. The result shows that the molar ratio of the composition at different temperatures is given in Table 2. The spectra indicate that both the samples are consistent with their elemental signals and stoichiometric is as expected. The corresponding peaks are due to the La, Sr, Mn, O elements, whereas no additional impurity peaks is detected and it implicit that the prepared samples in creation. This is almost consistent with the nominal composition suggesting that the obtained LSMO sample is near stoichiometric.

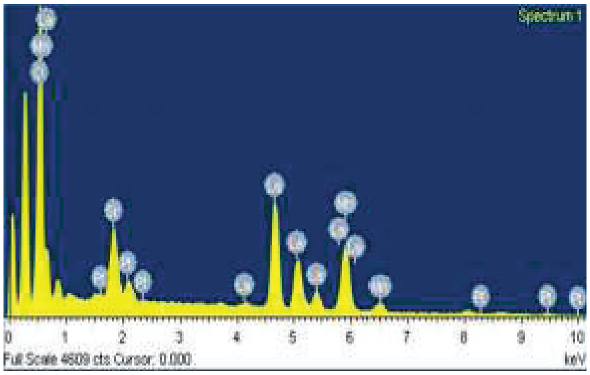

FIGURE 2. EDAX pattern of $La_{0.7}Sr_{0.3}MnO_3$sintering at different temperatures at 1250 and 1350°C

TABLE 2. Composition obtained from EDAX spectra.

Sample	SM0312	SM0313
La	19.3	19.4
Sr	1.91	1.99
Mn	19.61	19.7
O	58.57	58.5
Pt	0.61	0.41
Total	100	100

The morphology of the nanocrystalline LSMO powder was analyzed by field emission gun –scanning microscopy (FEG-SEM) using a JEOL-JSM-7600F. The FEG-SEM images of the powder sintered at different temperatures with the magnification of 20,000 are shown in Fig. 3(a) and 3(b).

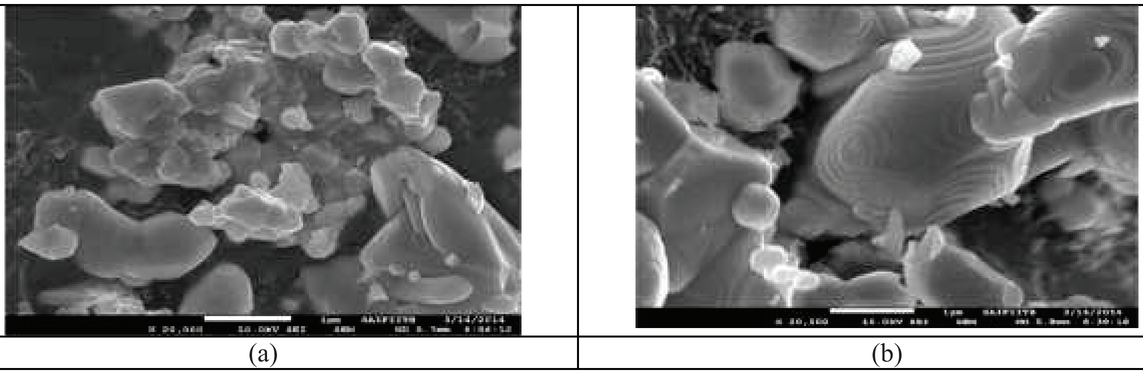

(a) (b)

FIGURE 3 (a), (b). FEG-SEM image of $La_{0.7}Sr_{0.3}MnO_3$sintering at different temperatures at 1250 and 1350°C

It is clearly seen that the most of the grain sizes are distributed in the range of 50-200 nm, which are larger than the one estimated using Scherrer formula. However, it further confirms the nanocrystallity of samples. The grain size varies between several microns whereas grains of small size can also be formed with higher sintering temperature. However, we observed some new spherical structure at 1350°C. The similar feature is also observed by Throat et al [25].

CONCLUSION

In summary, we have successfully synthesized single crystalline phase $La_{1-x}Sr_xMnO_3$(x=0.3) nanoparticles by simple solid state reaction route with a significantly short reaction time. Pure phase perovskite is formed at 1250°C and 1350°C. XRD pattern analysis shows that the samples have perovskite structure R-3c symmetry. LSMO nanostructures with packed particles or crystallite sizes of 47-51nm, having well perovskite structure were obtained. The crystallite size, structural symmetry and surface morphology can be governed by the calcinations temperature. The result of FEG- SEM measurement of the studied compound indicates that the spherical particles in the range of 50-200 nm are formed. The EDAX result shows that the molar ratio of La, Sr, Mn and O is near stoichimetric.

ACKNOWLEDGEMET

Financial assistance from the UGC, New Delhi is highly acknowledged.

REFERENCES

1. R. V. Helmolt. J. Wecker, B. Holzapfel, L. Schultz and K. Samwer, Phys. Rev. Letter **71**, 2331-2333 (1993).
2. S. P. Liu, G. D. Tang, P. Hao, L. Q. Xu, Y. G. Zhang, W. H. Qi, X. Zhao, D. L. Hou and W. Chen, J. Appl. Physics **105**, 013905 (2009).
3. A. M H. Gosnet and J. P. Renard, J. Phys. D: Appl. Physics **36**, 127-150 (2003).
4. S. Jin, T. H. Tiefel, M. Maecormark, R. A. Fastnacht, R. Ramesh and L. H. Chen, Science **264**, 413-415 (1994).
5. M. Talati and P. K. Jha, Phys. Rev. B **74**, 134406 (2006).
6. C. N. Rao, R. Mahesh, A. K. Raychaudhuri and R. Mahendiran, J. Phys. Chem. Solid **59**, 487-501 (1998).
7. A. J. Upendra and J. S. Lee, Solid State Phenomena **119**, 275- 278 (2007).
8. M. Talati and P. K. Jha, Computational Mater. Science **37**, 58-63 (2006).
9. R. D. Sanchez, J. Rivas and C. Vazquez et al, Appl. Phys. Letter **68**, 134 (1996).
10. N. Zhang, W. Ding, W. Zhong, D. Xing and Y. Du, Phys. Rev. B **56,** 8138 (1997).
11. K. Wang, W. Song, T. Yu, B. Zhao, M. Pu and Y.Sun, Physica Status Solidi A **171,** 577-582, (1999).
12. T.Tsuchiya, T. Yoshitake, Y. Shimakawa, Y. Kubo, Y. Yamaguchi, T. Manabe, T. Kumagai and S. Mizuta, Appl. Phys. A Mater. Sci. & Processing **79**, 1537-1539 (2004).
13. P. Dey, T. K. Nath, S. K. Mandal and A. Das, Int. Journal of Modern Phys. B **23**, 4889-4905 (2009).
14. S. Vasseur, E. Duguet, J. Portier, G. Goglio, S. Mornet, E. Hadov, K. Knizek, M. Marysko, P. Veverka and E. Pollert, J. Magn. Magn.Material **302**, 315 (2006).
15. V. Uskokovic, A. Kosak and M. Drofenik, Mater. Letter **60**, 2620 (2006).
16. N. Astik and P. K. Jha, "Investigation of structural and electrical properties of mixed ferrite system," in *International Conference on Condensed Matter Physics ICCMP-2014,* AIP Conference Proceedings 1661, edited by R. Sharma *et al.* (American Institute of Physics, Melville, NY, 2015), pp. 070001-070003.
17. M. Mazaheri and M. Akhavan, Physica B **405**, 72-76 (2010).
18. H. Aono, H. Hirazawa, H. Naohara, T. Maehara, H. Kikkawa and Y. Watanabe, Mater Res Bull **40**, 1126-1135 (2005).
19. M. Venkatesan, S. Nawka, S. C. Pillai, J. M. D. Coey, J. Appl. Physics 93, 8023-8025 (2003).
20. P. G. Radelii, G. Iannone, M. Marezio, H. Y. Hwang, S. W. Cheong, J. D. Jorgensen and D. N. Argyriou, Phys. Rev. B **56**, 8265 (1997).
21. Ma. Oumezzine, O. Pena, S. Kallel, T. Guizouarn and M. Oumezzine, J. Alloy Compound **533**, 33- 40 (2012).
22. M. Gupta, R. K. Kotnala, W. Khan, A. Azam and A. H. Naqvi, J. Solid State Chemistry **204**, 205-212 (2013).
23. B. Z. Sun, L. L. He, T. F. Luo and C. H. Yan, Mater. Letter **50**, 1507-1510 (2005).
24. Z. Sadighi, A. Ataie and M.R. Barati, Powder Technology **249**, 412-418 (2013).
25. N. D. Thorat, K. P. Shinde, S. H. Pawar, K. C. Barick, C. A. Betty and R. S. Ningthoujam, Dalton Transactions **10**, 3060- 3071 (2012).